# Detection of bosenovae with quantum sensors on Earth and in space

Jason Arakawa®, 1,2,3,\* Joshua Eby®, 4,† Marianna S. Safronova®, 1,5,‡

Volodymyr Takhistov®, 2,3,6,4,§ and Muhammad H. Zaheer® 1, ||

¹Department of Physics and Astronomy, University of Delaware, Newark, Delaware 19716, USA

²International Center for Quantum-field Measurement Systems for Studies of the Universe
and Particles (QUP, WPI), High Energy Accelerator Research Organization (KEK),

Oho 1-1, Tsukuba, Ibaraki 305-0801, Japan

³Theory Center, Institute of Particle and Nuclear Studies (IPNS),

High Energy Accelerator Research Organization (KEK), Tsukuba 305-0801, Japan

⁴Kavli Institute for the Physics and Mathematics of the Universe (WPI),

The University of Tokyo Institutes for Advanced Study,

The University of Tokyo, Kashiwa, Chiba 277-8583, Japan

⁵Joint Quantum Institute, National Institute of Standards and Technology and the University of Maryland,

College Park, Maryland 20742, USA

(Received 26 July 2023; accepted 19 August 2024; published 10 October 2024)

In a broad class of theories, the accumulation of ultralight dark matter (ULDM) with particles of mass  $10^{-22}~{\rm eV} < m_\phi < 1~{\rm eV}$  leads to the formation of long-lived bound states known as boson stars. When the ULDM exhibits self-interactions, prodigious bursts of energy carried by relativistic bosons are released from collapsing boson stars in bosenova explosions. We extensively explore the potential reach of terrestrial and space-based experiments for detecting transient signatures of emitted relativistic bursts of scalar particles, including ULDM coupled to photons, electrons, and gluons, capturing a wide range of motivated theories. For the scenario of relaxion ULDM, we demonstrate that upcoming experiments and technology such as nuclear clocks as well as space-based interferometers will be able to sensitively probe orders of magnitude in the ULDM coupling-mass parameter space, challenging to study otherwise, by detecting signatures of transient bosenova events. Detection of a bosenova event may also give information about microphysics properties of  $\phi$  that would otherwise be difficult with typical direct detection methods. Our analysis can be readily extended to different scenarios of relativistic scalar particle emission.

# DOI: 10.1103/PhysRevD.110.075007

## I. INTRODUCTION

The influence of dark matter (DM), which constitutes ~85% of matter in the Universe, has been firmly established by astronomical observations (see, e.g., [1] for a review). With decades of searches for its nongravitational interactions, the nature of DM remains mysterious. A particularly well-studied scenario has been that of weakly interacting massive particles, with typical masses in the

\*Contact author: arakawaj@udel.edu †Contact author: joshaeby@gmail.com †Contact author: msafrono@udel.edu \*Contact author: vtakhist@post.kek.jp |Contact author: hani@udel.edu

Published by the American Physical Society under the terms of the Creative Commons Attribution 4.0 International license. Further distribution of this work must maintain attribution to the author(s) and the published article's title, journal citation, and DOI. Funded by SCOAP<sup>3</sup>. range of 1 GeV–100 TeV, often associated with theories attempting to address the hierarchy problem. A well-motivated DM paradigm that has been less explored is ultralight dark matter (ULDM) [2], where extremely low-mass ( $10^{-22}$  eV  $\lesssim m_{\phi} \lesssim 1$  eV) bosonic fields  $\phi$  behave as classical waves due to their high occupation numbers and large de-Broglie wavelengths.

There are a multitude of ways in which ULDM can interact with the Standard Model (SM), which has led to the recent development of a broad and diverse experimental search program [2–4]. Owing to the wide range of possible masses  $m_{\phi}$  of ULDM, a large number of experiments, including atomic clocks [5–10], optical cavities [11–13], optical interferometers [14,15], spectroscopy [16–18], tests of the equivalence principle (EP) [19,20], mechanical resonators [21], fifth force searches [22,23], gravitational wave detectors [24,25], and torsion balance experiments [26] are currently exploring the ULDM parameter space. Scalar DM that couples to the SM can cause tiny variations in the

fundamental constants due to the coherent oscillations of the DM background, providing key observables that have been extensively studied [3,27].

ULDM can generally coalesce into long-lived bound structures known as *boson stars* [28–30]. Such states can form through purely gravitational interactions [31,32] or through self-interactions [33–35], and at small-enough densities they are stable both under perturbations [36–39] and decay [40–47]. The full gamut of phenomenological implications and experimental signatures of boson stars has been poorly explored.

A stable boson star configuration can be understood as a balance between the (attractive) self-gravity of the ULDM particles and their (repulsive) gradient energy. This balance can be sustained as long as the star is relatively dilute, such that the contribution of self-interactions is negligible. However, if the mass of the star grows through merger events [48–53] and/or accretion of ULDM from the background [32,54,55], eventually the self-interactions contribute and, if they are attractive in nature, they can destabilize the star.

When the boson star begins to collapse, its density rapidly increases, as does the binding energy of the collapsing ULDM particles. As the size of the star approaches the Compton wavelength of the ULDM,  $2\pi/m_{\phi}$ , annihilations of the ULDM particles to relativistic ones rapidly deplete the energy of the collapsing star. This typically occurs far before the star reaches its Schwarzschild radius, and therefore the boson star does not collapse to a black hole [57–59]. The pressure resulting from the relativistic emission reverses the collapse, and, after a few collapse emission cycles [58], a large fraction of the boson star energy is emitted, and the cold ULDM that remains settles into a dilute, gravitationally bound configuration again. This explosion of relativistic ULDM that occurs at the endpoint of boson star collapse is known as a *bosenova*.

The bosenovae are a promising target for distinct direct ULDM searches. In previous work [60], some of us studied the bosenova signal in detail for the case of ULDM composed of axionlike (parity-odd) fields, finding that current and near-future experiments, e.g., those using LC-circuit-based detectors [61,62] like ABRACADABRA [63,64], SHAFT [65], and DM-Radio [66–68], could viably search for relativistic ULDM bursts from collapsing boson stars. This was possible both because the energy density in the burst could exceed the background density of DM,  $\rho_{\rm DM} \simeq 0.4~{\rm GeV/cm^3}$ , and because the wave spreading of the burst in flight led to a month to year-long signal that

was highly coherent over the duration of the burst in the detector.

As stressed in Ref. [60], axionlike fields generically exhibit a close relationship between the self-interaction coupling  $\lambda$  of the ULDM field and its couplings to the SM: both couplings are typically determined by the same scale  $f_a$ , the axion decay constant. While such a relationship is predictive, other scalar fields (e.g. parity-even fields or dilatons) can have independent distinct DM-SM and self-interaction couplings. This highlights the importance of general exploration of possible scenarios for scalar field bursts.

In this paper, building on previous work [60], we consider and develop a comprehensive methodology to analyze a general ultralight scalar (parity-even) field, and determine the prospects for detecting transient signals of relativistic scalars emitted in bosenovae. We describe the DM-SM interactions in effective field theory (EFT) with dilatonic couplings, e.g., with couplings to photons, electrons, and gluons, capturing a large swath of possible theories. Although most of the analysis is model independent, we also examine in detail the specific case of a *relaxion* field [69] as a concrete realization of the scalar DM with dilatonic couplings [70,71].

The paper is organized as follows. Section II outlines the leading-order couplings between the DM and the SM within the framework of EFT. We also include a detailed discussion of constraints on the self-interactions of ULDM. We proceed by describing boson stars and the properties of their explosions in Sec. III. Section IV discusses the detection prospects of the transient scalar bursts, and Sec. V presents the results, including general sensitivity analyses for photon, electron, and gluon couplings. We also analyze detection prospects in the scenario of relaxion DM. We reserve Sec. VI for our conclusions and future outlook. We work in natural units throughout with  $\hbar=c=1$ .

# II. EFFECTIVE COUPLINGS

# A. Dilatonic ULDM-SM couplings

We consider the case of DM as composed of a real scalar field  $\phi$ . Direct scalar couplings of  $\phi$  with the SM can lead to an effective variation of fundamental constants, which are targets for direct searches (e.g., in quantum sensors) as discussed in the Introduction (see, e.g., [19]). Such operators can be characterized within EFT as

$$\mathcal{L}_{\text{int}} = \sum_{n,i} d_i^{(n)} \left(\frac{\phi}{M_{\text{pl}}}\right)^n \mathcal{O}_{\text{SM}}^i, \tag{1}$$

where  $d_i^{(n)}$  are the dilatonic couplings labeled by an index i and  $\phi$ -exponent n, and  $\mathcal{O}_{\text{SM}}^i$  are corresponding operators within the SM. The leading effective couplings, which appear at linear order (n=1), are

<sup>&</sup>lt;sup>1</sup>This discussion holds when the boson star is still nonrelativistic when the self-interactions become relevant. Note on the contrary that, if the self-interactions are exceptionally weak, then the boson star can become a black hole directly as a result of mass increase. See the discussion in Sec. III. In the special case of ULDM axions with Planck-scale decay constants, these conclusions can also be modified [47,56].

$$\mathcal{L}_{\text{int}} \supset \frac{\sqrt{4\pi}\phi}{M_{\text{pl}}} \left( d_{m_e}^{(1)} m_e \bar{e} e + \frac{d_e^{(1)}}{4} F_{\mu\nu} F^{\mu\nu} + \frac{d_g^{(1)}\beta(g_s)}{2g_s} G_{\mu\nu}^a G^{a\mu\nu} \right), \tag{2}$$

where e is the electron field with mass  $m_e$ ,  $F^{\mu\nu}$ , and  $G^{a\mu\nu}$  are the photon and gluon field strength tensors (respectively), and  $g_s$  and  $\beta(g_s)$  are the coupling and beta function of QCD. The three interaction terms above lead to effective variation of fundamental quantities (respectively): the electron-to-proton mass ratio  $m_e/m_p$ , the fine-structure constant  $\alpha$ , and the strong coupling constant  $\alpha_s$ .

In this work, we focus on the linear-in- $\phi$  couplings given in Eq. (2). However, we note that a family of operators of higher dimensionality exists as well. The next-to-leading-order couplings are quadratic in  $\phi$ , and can have interesting phenomenological consequences [19,72,73]. A qualitative difference between linear and quadratic couplings is that the latter can lead to screening (or antiscreening) of the field in the presence of significant matter densities (see [19] for details). This could suppress (or enhance) detection sensitivities for terrestrial experiments, even when the detection sensitivity is otherwise dominated by the leading-order coupling. This additional model dependence provides one motivation for the use of space-based experiments [72].

## **B. ULDM self-interactions**

In addition to the ULDM-SM interaction Lagrangian of Eq. (2), we parametrize the  $\phi$ -only Lagrangian as

$$\mathcal{L}_{\phi} = \frac{1}{2} \partial_{\mu} \phi \partial^{\mu} \phi - \frac{1}{2} m_{\phi}^2 \phi^2 + \frac{\lambda}{4!} \phi^4 + \cdots. \tag{3}$$

Generically,  $\lambda$  can be positive or negative, corresponding to attractive and repulsive self-interactions (respectively). We focus on the case of attractive self-interactions, as the collapse of boson stars (which gives rise to the signal we are investigating) only arises when  $\lambda > 0$  [37–39]. Attractive self-interactions can generically be realized within ultraviolet (UV) completions (see, e.g., [74]).

We note that a cubic term,  $-\lambda_3\phi^3/3!$ , is possible as well, and can be attractive or repulsive. However, its leading contribution is to mediate  $2 \to 1$  or  $1 \to 2$  transitions which are suppressed in the nonrelativistic limit relevant to DM studies. For simplicity, in this work we set  $\lambda_3 = 0$  and focus on  $\lambda$ . In boson star collapse, the presence of this cubic term or terms proportional to  $\phi^n$  with n > 4 may modify the emission spectrum of bosons in the bosenova, which is a topic we leave for future work. See Sec. III for a brief discussion.

The couplings considered in this work are extremely small,  $\lambda \ll 1$ , as motivated by well-studied models of ULDM. As a benchmark example, axionlike fields often

have self-interaction couplings determined by their mass  $m_{\phi}$  and symmetry-breaking scale  $f_a$  as  $\lambda \simeq (m_{\phi}/f_a)^2$ . For QCD axions, one has  $m_{\phi}f_a \simeq \Lambda_{\rm QCD}^2 \simeq (75 \ {\rm MeV})^2$  (the QCD scale; see, e.g., [75]), implying  $\lambda \simeq m_{\phi}^4/\Lambda_{\rm QCD}^4 \simeq 3 \times 10^{-56} (m_{\phi}/\mu {\rm eV})^4$ . Studies of so-called fuzzy DM [76–80] often use a benchmark of  $m_{\phi} \simeq 10^{-22} \ {\rm eV}$  and  $f_a \simeq 10^{16} \ {\rm GeV}$ , which gives  $\lambda \simeq 10^{-94}$  (see [81,82] for recent reviews). We will discuss constraints on  $\lambda$  in the next section.

Note that for axionlike fields, the SM couplings are typically connected to the same high scale  $f_a$ . For example, the linear axion-photon interaction is typically parametrized as  $\mathcal{L}_{a\gamma} \propto (\phi/f_a) F^{\mu\nu} \tilde{F}_{\mu\nu}$ , where  $\tilde{F}$  is the dual field strength of the photon. This relation is not applicable to the scalars considered in this work.

#### C. Constraints on $\lambda$

In parametrizing the scalar field EFT, we treat  $\lambda$  as independent of the SM couplings at the Lagrangian level (in contrast to the axion case just described). Therefore, it is useful to explore general constraints on  $\lambda$ , which we describe below and summarize in Fig. 1.

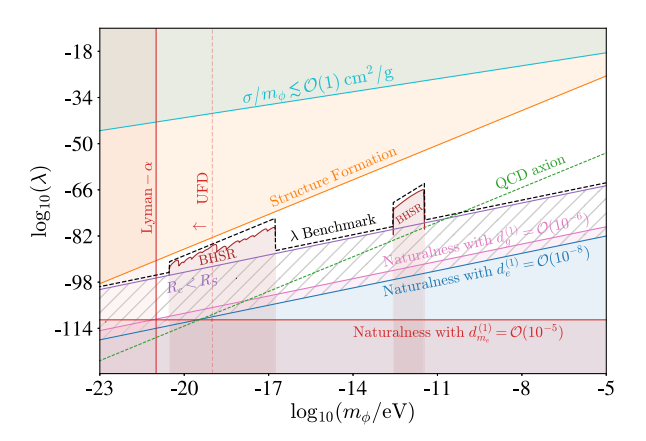


FIG. 1. Summary of the parameter space relevant for the bosenova signal analyzed in this work. Constraints on  $\lambda$  illustrated arise from the bullet cluster (cyan) [83], structure formation (orange) [84], Lyman- $\alpha$  [85,86] and UFD galaxies [87] (red vertical thick and dashed lines, respectively), black hole superradiance [88,89] (BHSR, brown), as well as the lower bounds for naturalness arising from  $d_e$  (blue),  $d_{m_e}$  (red), and  $d_q$  (pink). The naturalness lines assume benchmark values for the couplings which are allowed by current experiments, as labeled. We also illustrate the region where critical boson stars would not undergo bosenova due to general relativistic effects (purple hatched region). The dashed black line represents the benchmark values for  $\lambda$  that we choose at each mass, as given in Eq. (40) and explained in Sec. V. Finally, for comparison, we show the QCD axion line corresponding to  $|\lambda| \simeq m_{\phi}^4/\Lambda_{\rm OCD}^4$  (green dotted line); see text for details.

## 1. Bullet cluster

The coupling  $\lambda$  can be constrained by the observed gross distribution of DM in galaxy-cluster collisions, including the bullet cluster [83]. The tree-level scattering cross section  $\sigma$  for  $\phi - \phi$  scattering via  $\lambda$  is given by

$$\frac{\sigma}{m_{\phi}} = \frac{\lambda^2}{16\pi m_{\phi}^3}.\tag{4}$$

Gravitational-lensing observations of the bullet cluster constrain the DM self-interaction cross section to be [83]

$$\frac{\sigma}{m_{\phi}} \lesssim \mathcal{O}(1) \text{ cm}^2/\text{g},$$
 (5)

which implies

$$\lambda \lesssim 10^{-11} \left(\frac{m_{\phi}}{\text{eV}}\right)^{3/2}.\tag{6}$$

This model-independent constraint on DM self-interactions is illustrated by the cyan shaded region in Fig. 1.

# 2. Cosmological constraints

The presence of ultralight fields of mass m and self-interaction coupling  $\lambda$  gives rise to contributions to the evolution of the matter power spectrum, as discussed in, e.g., [27,74]. Density perturbations  $\delta_{\bf k} \equiv (\rho_{\bf k} - \bar{\rho})/\bar{\rho}$  at scales  $|{\bf k}|$  will evolve as

$$\ddot{\delta}_{\mathbf{k}} + 2H\dot{\delta}_{\mathbf{k}} \simeq \left[ \frac{4\pi\bar{\rho}}{M_{\rm pl}^2} - \left( \frac{\mathbf{k}^2}{4m_{\phi}^2 a^2} - \frac{3\lambda\phi^2}{16m_{\phi}^2} \right) \frac{\mathbf{k}^2}{a^2} \right] \delta_{\mathbf{k}}, \quad (7)$$

where H is the Hubble parameter, a is the scale factor of the Universe, and  $\bar{\rho}$  and  $\rho_{\bf k}$  are the average DM density and the density at scale  $|{\bf k}|$  (respectively). The first term in parentheses on the right-hand side of Eq. (7) contributes to a suppression of the matter power spectrum on a distance scale of  $L_m \simeq [\pi^3 M_{\rm pl}^2/(\bar{\rho} m_\phi^2)]^{1/4}$ . In the mass range  $m_\phi \lesssim 10^{-21} - 10^{-20}$  eV, this can lead to constraints from measurements of small-scale structure in Lyman- $\alpha$  forest [85,86]. A stronger constraint, approximately  $m_\phi \gtrsim 10^{-19}$  eV, was recently derived in Ref. [87] by modeling stellar velocity dispersion in ultra-faint dwarf (UFD) galaxies. The result depends on astrophysical assumptions about the evolution and tidal stripping of DM in particular UFDs (see, e.g., [90]). These constraints are illustrated by the red thick and dashed lines (respectively) in Fig. 1.

The second term in parentheses on the right-hand side of Eq. (7) suppresses (enhances) the matter power spectrum when  $\lambda < 0$  ( $\lambda > 0$ ), corresponding to a repulsive (attractive) interaction; the relevant scale is approximately  $L_{\lambda} \simeq [3\pi |\lambda| M_{\rm pl}^2/(8m_{\phi}^4)]^{1/2}$ . Observational constraints

require  $L_{\lambda} \lesssim \text{Mpc}$  [84], corresponding to

$$\lambda \lesssim 3 \times 10^{-79} \left( \frac{m_{\phi}}{10^{-18} \text{ eV}} \right)^4.$$
 (8)

We show this constraint in orange color in Fig. 1. Note that these constraints may be improved due to enhancement of the power spectrum before matter-radiation equality (see discussion in [91]). Additionally, there are constraints on the lowest masses of dark matter  $m_{\phi} \lesssim 10^{-21}$  eV from studies of the concentration of dark matter in the Galactic Center [92,93].

Note finally that the constraints of this section and the previous one assume that  $\phi$  constitutes an  $\mathcal{O}(1)$  fraction of the DM of the Universe, and vanish when this is not so.

# 3. Naturalness of $\lambda$

We also consider theoretical constraints on  $\lambda$ , demanding that the values of  $\lambda$  considered do not require technical finetuning of the theory (see, e.g., [94] for a recent summary). The  $\phi$ -SM couplings can generate self-interactions proportional to  $\phi^4$  through box diagrams, illustrated in Fig. 2 for electron (upper) or gauge boson (lower) couplings. If this contribution is much larger than the physical, observable  $\lambda$ , then this implies an "unnatural" cancellation between the loop contribution and the bare Lagrangian parameter, which are *a priori* unrelated. This allows us to set an approximate lower bound on the value on  $\lambda$ , essentially by the requirement that the effective  $\lambda$  coupling is not much smaller than the one generated at one loop.

Integrating the box diagrams in Fig. 2 up to some UV cutoff  $\Lambda_{\rm UV}$  gives

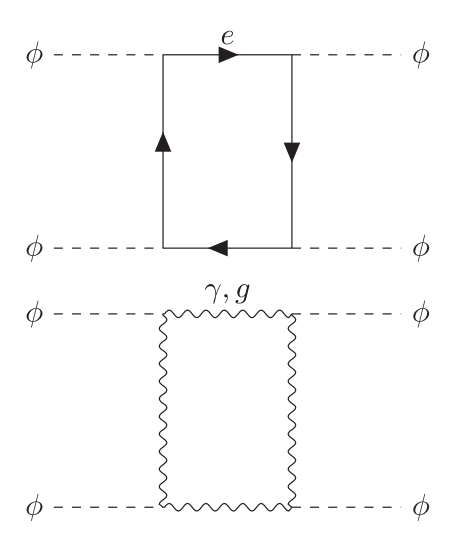


FIG. 2. One-loop diagrams that generate corrections to  $\lambda$  from the linear  $\phi$  coupling  $d_{m_e}^{(1)}$  (upper panel) or  $d_e^{(1)}$  and  $d_g^{(1)}$  (lower panel).

$$\lambda(\Lambda_{\text{UV}}) \simeq \lambda(\mu_0) - \frac{(d_{m_e}^{(1)})^4 m_e^4}{8\pi^2 M_{\text{pl}}^4} \log\left(\frac{\Lambda_{\text{UV}}}{\mu_0}\right) + \frac{(d_e^{(1)})^4}{32\pi^2 M_{\text{pl}}^4} \Lambda_{\text{UV}}^4 + \frac{(d_g^{(1)}\beta(g_s))^4}{2\pi^2 g_s^4 M_{\text{pl}}^4} \Lambda_{\text{UV}}^4, \quad (9)$$

where  $\mu_0$  is some reference energy scale. Equation (9) represents a rough estimate for illustration only; the gluon coupling in particular neglects any color factors that may alter the expression by an  $\mathcal{O}(1)$  factor.

In its current form, each term of Eq. (9) has two unknown parameters:  $d_i^{(1)}$  and  $\Lambda_{\rm UV}$ . To obtain a definitive bound on  $\lambda$  from this expression, we also need a constraint on  $\Lambda_{\rm UV}$ , especially for the gauge boson loops, which are quartic in  $\Lambda_{\rm UV}$ . As noted in Ref. [73], there is an upper bound on the UV cutoff of the theory from requiring that the one-loop mass corrections induced by the DM-SM interactions are also natural. Since the interactions involved in the corrections to  $m_\phi^2$  and  $\lambda$  are the same, the UV scales that arise in loop integration are the same. The loops have quadratic and quartic UV divergences, which means that the UV cutoff must be sufficiently small for the mass corrections to be subdominant to the tree-level mass of  $\phi$  [72]. By enforcing  $\delta(m_\phi^2) \lesssim m_\phi^2$ , we obtain

$$\Lambda_{\rm UV}^{m_e} \lesssim 2^{3/2} \frac{\pi m_\phi M_{\rm pl}}{d_{m_e}^{(1)} m_e},$$
 (10)

$$\Lambda_{\rm UV}^e \lesssim 2^{5/4} \sqrt{\frac{\pi m_\phi M_{\rm pl}}{d_e^{(1)}}},$$
(11)

$$\Lambda_{\rm UV}^g \lesssim 2^{3/4} \sqrt{\frac{\pi m_\phi M_{\rm pl} g_s}{d_g^{(1)} \beta(g_s)}},\tag{12}$$

for the electron, photon, and gluon couplings respectively. Substituting these limits on the UV cutoff into the renormalized  $\lambda$  in Eq. (9), we find

$$\lambda \gtrsim \frac{(d_{m_e}^{(1)})^4 m_e^4}{8\pi^2 M_{\rm pl}^4} \log\left(\frac{\sqrt{8\pi m_\phi} M_{\rm pl}}{d_{m_e} \mu_0}\right),$$
 (13)

$$\lambda \gtrsim (d_e^{(1)})^2 \frac{m_\phi^2}{M_{\rm pl}^2},\tag{14}$$

$$\lambda \gtrsim 2 \left( d_g^{(1)} \frac{\beta(g_s)}{g_s} \right)^2 \frac{m_\phi^2}{M_{\rm pl}^2},\tag{15}$$

for the electron, photon, and gluon couplings, respectively. Therefore, the "natural" regions of  $\lambda$  depend on the unknown SM couplings. For illustration, in Fig. 1 we show the natural scale of  $\lambda$  assuming  $d_e^{(1)} = 10^{-8}$ ,  $d_{m_e}^{(1)} = 10^{-5}$ ,

and  $d_q = 10^{-6}$  (blue, red, and pink, respectively), which are benchmark values that are allowed by current constraints across the full range of  $m_{\phi}$  we consider in this work (cf. the results of Sec. V). For the electron coupling in Fig. 1, we assume  $\log(\sqrt{8}\pi m_{\phi}M_{\rm pl}/d_{m_e}^{(1)}\mu_0) \sim \mathcal{O}(1)$ , as the prefactor primarily determines its magnitude. For the gluon coupling, the  $\beta$  function is given by  $\beta(g_s)/g_s =$  $-(11 - n_s/6 - 2n_f/3)g_s^2/16\pi^2$ . Here we use  $\alpha_s \equiv$  $q_s^2/4\pi = 1$  to represent that QCD is nonperturbative at these energy scales. The results do not strongly depend on the value chosen for  $\alpha_s$ , and the  $R_c > R_S$  constraint (purple region) discussed below, where  $R_S$  is the Schwarzschild radius, is strictly stronger. Even for a choice of larger benchmark couplings limited by the EP bounds, the  $R_c > R_S$  constraint remains stronger. Additionally, we do not specify a UV completion, which could modify  $\beta(g_s)$  via the introduction of additional  $SU(3)_c$  colored scalars  $(n_s)$ and fermions  $(n_f)$ , but this also does not appreciably change the results shown here. For simplicity, we choose the SM contribution  $n_s = 0$  and  $n_f = 6$ .

# 4. Black hole superradiance

In the vicinity of a rapidly rotating black hole, ultralight scalars can be produced in hydrogenlike bound states by extracting energy and angular momentum from the black hole. This process, known as *black hole superradiance*, is most efficient for scalars whose Compton wavelength is comparable to the Schwarzschild radius of the black hole, i.e.,  $2\pi m_{\phi}^{-1} \simeq R_S \equiv 2M_{\rm BH}/M_{\rm pl}^2$ , where  $M_{\rm BH}$  is the black hole mass [95–97].

Because superradiance causes the host to spin down over time, observations of black holes with large spins today have led to constraints on the existence of such scalars, in the mass range  $m_{\phi} \simeq 10^{-13} - 10^{-11}$  eV (for solar-mass black holes) [88] and  $m_{\phi} \simeq 10^{-21} - 10^{-17}$  eV (for supermassive black holes) [89]. We illustrate these constraints by the brown lines in Fig. 1. These studies take advantage of a large number of measured black hole spins, which are difficult to measure and in some cases have  $\mathcal{O}(1)$  uncertainties, and are likely to improve in the future. Direct laboratory searches, including those studied here, are complementary to these indirect astrophysical limits.

Self-interactions can also lead to important effects on black hole superradiance, as the constraints in Fig. 1 illustrate. If the scalar field density around the black hole exceeds a critical value, attractive self-interactions destabilize the cloud, causing it to collapse and quenching its exponential growth [95]. Depending on the value of the self-interaction coupling  $\lambda$ , the cloud can also transition to a steady-state configuration, where superradiant states are excited and relaxed at roughly equal rates [88,98]. This also quenches the growth of the cloud. The end result of both processes is that, for strong-enough self-interaction couplings, the superradiance rate is insufficient to spin down

the black hole on astrophysical timescales, and the constraints are relaxed accordingly. Roughly, spin-down occurs within the lifetime of the Universe when [98]

$$|\lambda| < 10^{-64} \alpha_g \left(\frac{m_\phi}{10^{-10} \text{ eV}}\right)^{5/2},$$
 (16)

though this condition is approximate and only valid when the gravitational coupling  $\alpha_g \equiv M_{\rm BH} m_\phi/M_{\rm pl}^2$  is order unity for a given  $M_{\rm BH}$ . A full study of the spin-down rates gives rise to the upper edge of the superradiance constraints seen in [88,89], reproduced in Fig. 1.

# D. Relaxion dark matter

As a concrete example of a well-motivated particle physics model that is captured by our analysis, consider the relaxion, a scalar field proposed to alleviate the hierarchy problem in the Higgs sector [69]. In these models, the cosmological rolling of the  $\phi$  (relaxion) field scans the electroweak scale  $v_{\rm ew}$  until a Higgs-dependent backreaction traps  $\phi$  in a local minimum with a Higgs mass scale close to the measured value. Additionally, by displacing the relaxion field from the minimum of its potential, either by reheating the Universe after inflation [70] or through stochastic quantum fluctuations [71], the relaxion is able to acquire a significant energy density, making it a viable ULDM candidate.

Because the backreaction potential is generated through direct  $\phi$ -Higgs couplings, the relaxion naturally acquires Higgs-like interactions with SM fields parametrized by an effective scalar mixing angle  $\theta_{h\phi}$  (see, e.g., [99] for details). We therefore characterize the effective relaxion couplings with a Lagrangian of the form

$$\mathcal{L} \supset \sin \theta_{h\phi} \frac{\phi}{\sqrt{2}} \left( \sum_{f} \frac{m_{f}}{v_{\text{ew}}} \bar{f} f + c_{\gamma} \frac{\alpha}{4\pi v_{\text{ew}}} F_{\mu\nu} F^{\mu\nu} + c_{g} \frac{\alpha_{s}}{4\pi v_{\text{ew}}} G^{a}_{\mu\nu} G^{a\mu\nu} \right), \tag{17}$$

where f is a SM fermion field (we will take f = e in what follows). Comparing each term to the EFT parametrization in Eq. (2), we can derive the relationship of  $\sin \theta_{h\phi}$  to each of the dilatonic couplings  $d_i^{(1)}$ :

$$\sin \theta_{h\phi} = \frac{v_{\text{ew}}}{M_{\text{pl}}} \times \begin{cases} \sqrt{8\pi} d_{m_e}^{(1)} & (\text{electron}) \\ \frac{\sqrt{8\pi^3}}{\alpha} d_e^{(1)} & (\text{photon}) \\ \frac{\sqrt{8\pi^2} \beta(g_s)}{a_s^{3/2}} d_g^{(1)} & (\text{gluon}) \end{cases} , \quad (18)$$

where for simplicity we took  $c_{\gamma}=c_g=1$ . As with axion-like fields, relaxion self-interactions can be parametrized by the effective coupling  $\lambda \simeq m_{\phi}^2/f_a^2$ . Nonetheless, taking  $f_a$ 

as a free parameter, this implies that  $\lambda$  can take a wide range of values in the allowed region of Fig. 1.

#### III. BOSON STARS

ULDM can form self-gravitating bound states known as boson stars [28–30], which can be understood as quasistatic standing-wave solutions of the low-energy equations of motion: the Gross-Pitaevskii–Poisson (GPP) equations [37,38]. These equations are easily derived from the relativistic Lagrangian in Eq. (3) (minimally coupled to gravity) by decomposing the ULDM field  $\phi$  using  $\phi = [\psi \exp(-im_{\phi}t) + \text{H.c.}]/\sqrt{2m_{\phi}}$  with  $\psi$  a nonrelativistic wave function, and neglecting higher-order terms in the limit  $\ddot{\psi} \ll m_{\phi} \dot{\psi} \ll m_{\phi}^2 \psi$ . After a short derivation (see, e.g., [100,101]), the resulting GPP equations are

$$i\dot{\psi} = \left(-\frac{\nabla^2}{2m_{\phi}} + V_g(|\psi|^2) - \frac{\lambda}{8m_{\phi}^2}|\psi|^2\right)\psi,$$
 (19)

$$\nabla^2 V_a = 4\pi G m_b^2 |\psi|^2,\tag{20}$$

where  $V_g(|\psi|^2)$  is the self-gravitational potential. When the density  $|\psi|^2$  is relatively small, the third term in Eq. (19) (which arises from self-interactions and is proportional to  $\lambda$ ) can be neglected, and the boson star is understood as a stable balance of the other two forces.

As the mass of a boson star grows, its density also grows, and the attractive self-interaction of the field becomes stronger. Once it is of the same order as the other terms in Eq. (19), this interaction destabilizes the star, leading to gravitational collapse. This occurs once the boson star reaches a critical value of the mass  $M_c \approx 10 M_{\rm pl}/\sqrt{\lambda}$  [37,38]. The corresponding (minimum) radius of a boson star is  $R_c \approx 0.5 M_{\rm pl} \sqrt{\lambda}/m_{\phi}^2$ .

As a consequence of the above, at the critical point (just before it collapses), the radius and mass of a boson star are related as

$$R_c \approx \frac{5M_{\rm pl}^2}{M_c m_\phi^2}.$$
 (21)

In Fig. 3, we show the mass-radius relationship of critical boson stars in Eq. (21) for different choices of the  $m_{\phi}$  (blue lines, as labeled). The gray regions represent masses and radii of boson stars that are either more massive or larger than the Milky Way itself. The red region represents the region where the detection of bosenovae is disfavored because the density of the boson star  $\rho_c \simeq 3 M_c/(4\pi R_c^3) < \rho_{\rm DM}$ .

Importantly, the allowed mass-radius relationship for critical boson stars in Eq. (21) was derived in the nonrelativistic limit. As  $m_{\phi}$  increases, the critical radius  $R_c$  becomes

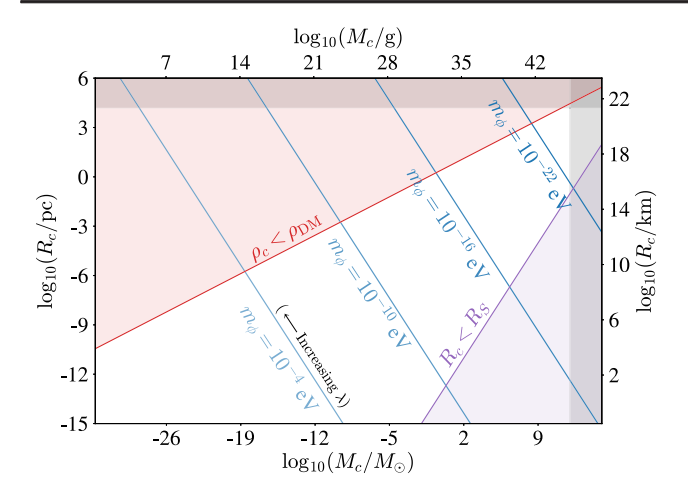


FIG. 3. Mass-radius relation of scalar boson stars along the critical point in Eq. (21) for different values of the scalar mass,  $m_{\phi}$  (blue lines, as labeled). The red shaded region is disfavored from the perspective of detection, as in this region, the density of a boson star is smaller than the ambient DM density. Additionally, the two gray shaded regions signify where the boson stars either become larger ( $\gtrsim 16$  kpc), or more massive ( $\gtrsim 10^{12} M_{\odot}$ ) than the Milky Way Galaxy. The purple shaded region represents the Schwarzschild limit, where boson stars will not explode; see Sec. III for details.

smaller, eventually approaching the Schwarzschild radius of the boson star,  $R_S \equiv 2M_c/M_{\rm pl}^2$ ; at this point, the non-relativistic calculation would suggest that the boson star forms a black hole, though in fact the calculation breaks down unless  $R_c \ll R_S$ . Using Eq. (21), we can interpret this as a limitation on the critical mass as a function of  $m_\phi$ ,

$$M_c \gtrsim \sqrt{\frac{5}{2}} \frac{M_{\rm pl}^2}{m_{\phi}},\tag{22}$$

or equivalently, a minimum value of  $\lambda$ ,

$$\lambda \gtrsim \lambda_{\rm BH} \equiv 40 \frac{m_{\phi}^2}{M_{\rm pl}^2},\tag{23}$$

for which our study is applicable.

We illustrate this region of parameter space in purple color in both Figs. 1 and 3. In the shaded range, the equation of state is dominated by general-relativistic corrections, and the analysis above no longer applies. On the basis of previous work [47,56–59], we expect no bosenova to take place in this regime. Note that this applies, for example, to QCD axion stars for  $m_{\phi} \lesssim 10^{-10}$  eV (see green dotted line in Fig. 1).

## A. Bosenova signal

As described in the Introduction, very massive boson stars (with mass approaching  $M_c$ ) collapse gravitationally

due to the attractive  $\phi^4$  self-interaction in Eq. (3). In the final stage of boson star collapse, relativistic number-changing processes in the core of the collapsing star are excited, and high-energy ULDM particles are rapidly emitted from the star [57,58]. This process is known as a *bosenova*, by analogy to supernovae observed from the collapse of heavy stars. The "life-cycle" of a boson star (including mass growth, collapse, and bosenova) is illustrated in Fig. 4.

A full-scale simulation of the collapse, including relativistic evolution and eventual bosenova, was conducted in [58]. The authors found that the leading relativistic peak in the emission spectrum was centered near the momentum of  $^2$   $\bar{k} \simeq 2.4 m_{\phi}$ , with width  $\delta k \simeq m_{\phi}$ . The total integrated energy emitted around this leading peak was of order

$$\mathcal{E}_{\text{peak}} \approx 1020 \frac{m_{\phi}}{\lambda},$$
 (24)

where we translated the result of Ref. [60] but substituted  $\lambda = m_\phi^2/f_a^2$ . In the simulation, the boson star collapsed and exploded  $\mathcal{O}(\text{few})$  times before eventually settling to a stable, dilute configuration; each collapse produced an energy of order  $\mathcal{E}_{\text{peak}}$  on a timescale of order  $\delta t_0 \simeq 400/m_\phi$ , corresponding to an intrinsic burst "size" of  $\delta x_0 \simeq 400/m_\phi$  (since the scalar velocity is  $v_* \simeq 1$ ). This work focuses on the signal from a single explosion, and is in this sense conservative, as the signal should only be enhanced by additional subsequent explosions.

Note that the authors of [58] analyzed the emission spectrum for axionlike fields with a chiral potential, i.e., a QCD axion (see, e.g., [75]). The leading term in this potential has the same form as we consider in Eq. (3). Although we are considering a different set of physical models, we will employ the output of these simulations as a characteristic behavior for the present study. Indeed, the authors of [58] indicate that in their simulations, they did not observe a strong dependence of the emission spectrum on the specific form of the potential, and since we are considering only the leading relativistic peak (which should be dominated by the  $\phi^4$  term), we expect the difference to be small at leading order.

The precise form of the potential, including higher-order terms, could affect detection prospects. It is an open question, a detailed study of which we leave for future work, whether differences in the emission spectrum arising from distinct self-interaction potentials can be distinguished experimentally. In the event of a detection, such details could contain important information about the underlying scalar field theory, including its UV completion, which could be challenging to probe otherwise.

<sup>&</sup>lt;sup>2</sup>This peak can be understood as arising from a leading  $3\phi \rightarrow \phi$  number-changing interaction which is  $\infty\lambda$ ; see, e.g., [41,44,57].

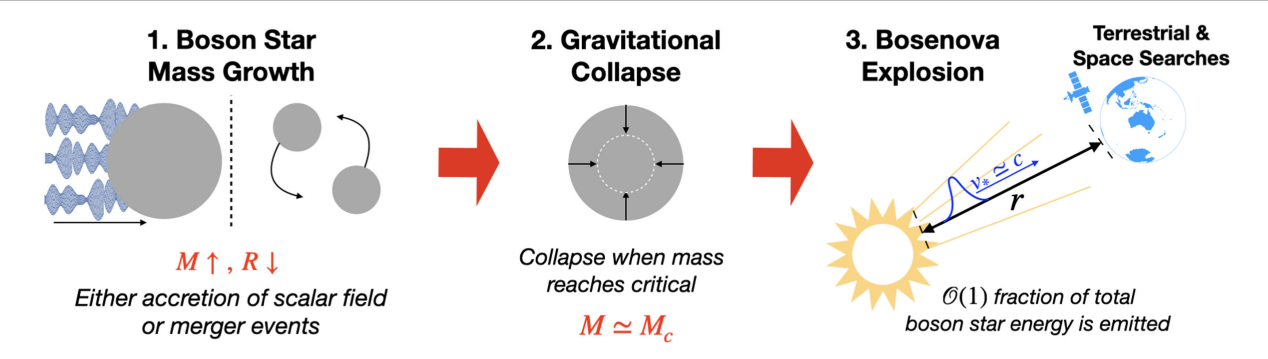


FIG. 4. Illustration of the basic process leading to the signal analyzed in this work, which divides into three subprocesses: (1) the boson star mass M grows by accretion or merger, until (2) M approaches the critical value  $M_c$ , leading to spherical collapse. Finally, (3) in the final moments of collapse, the collapsing scalar field density grows large, exciting rapid emission of relativistic scalars in a *bosenova* explosion. See text for further details.

Bosenovae eject bursts of relativistic ULDM bosons in an approximately spherical shell, which can eventually reach Earth. Under the assumption that the thickness bosenova shell  $\delta x$  is much smaller than the distance from the explosion to Earth,  $\delta x \ll r$ , the energy density in a bosenova shell is

$$\rho_* \approx \frac{\mathcal{E}}{4\pi r^2 \delta x},\tag{25}$$

where  $\mathcal{E}$  is the total energy emitted in the burst. If the emitted scalar waves do not spread in flight, then the duration of the burst is merely the intrinsic duration from the source,  $\delta x \to \delta x_0$ . Using this result and substituting  $\mathcal{E} = \mathcal{E}_{\text{peak}}$  from Eq. (24), one finds

$$\rho_{*,0} \simeq 4 \times 10^8 \rho_{\rm DM} \left( \frac{m_\phi}{10^{-15} \text{ eV}} \right)^2 \left( \frac{10^{-80}}{\lambda} \right) \left( \frac{\text{pc}}{r} \right)^2$$
 (26)

in the limit of minimal wave spreading. However, as the shell propagates to Earth, the wave naturally spreads in flight. This further dilutes the energy density by the factor [60]

$$\frac{\delta x_0}{\delta x} \simeq \left(\frac{\xi^2 q(q^2+1)}{1.5 \times 10^8}\right) \left(\frac{10^{-15} \text{ eV}}{m_\phi}\right) \left(\frac{\text{pc}}{r}\right),$$
 (27)

where  $\xi \equiv m_{\phi} \delta x_0 \approx 400$ , and  $q \equiv \bar{k}/m_{\phi} \approx 2.4$ , and we took  $\delta k \simeq m_{\phi}$ . Therefore, at the detector, the energy density takes the form

$$\frac{\rho_*}{\rho_{\rm DM}} \simeq \frac{\rho_{*,0}}{\rho_{\rm DM}} \frac{\delta x_0}{\delta x} \simeq 3 \left( \frac{m_\phi}{10^{-15} \text{ eV}} \right) \left( \frac{10^{-80}}{\lambda} \right) \left( \frac{\text{pc}}{r} \right)^3. \quad (28)$$

We conclude that the energy density in the burst at the position of Earth can be much larger than the ambient DM density  $\rho_{\rm DM} \simeq 0.4~{\rm GeV/cm^3}$ .

On the other hand, the oscillations of the scalar waves are very incoherent at the source [with  $\mathcal{O}(m_{\phi})$  spread in

momentum], compared to the high-quality oscillations of the ambient DM (which has a momentum spread  $\propto m_{\phi}v_{\rm DM}^2 \simeq 10^{-6}m_{\phi}$ ). However, as pointed out in [60], the spreading of the waves leads to increased effective coherence in the detector. This can be understood by observing that the different momentum modes travel at different velocities, e.g., with the fastest modes arriving first, so at any given time the energy deposition in the detector is remarkably coherent. It was found that the *effective* coherence time of a relativistic burst at the detector scaled as

$$\tau_* \simeq \frac{2\pi r}{q^3 \xi} \simeq 4 \times 10^{-3} \text{ year}\left(\frac{r}{\text{pc}}\right),$$
 (29)

which approaches, e.g., 1 year for  $r \simeq 300$  pc. The duration of the burst is also extended, as

$$\delta t \simeq \frac{\delta k}{m_{\phi}} \frac{r}{q^2 \sqrt{q^2 + 1}} \simeq 0.2 \text{ year} \left(\frac{r}{\text{pc}}\right),$$
 (30)

where as before we took  $\delta k \simeq m_\phi$ . For the two benchmark distances we consider, the signal durations are estimated to be a few months for r=1 pc, and  $\mathcal{O}(100 \text{ years})$  for r=1 kpc. This significant momentum spread implies that broadband, rather than resonant, searches for ULDM are optimal for bosenova searches. We note that even though the signal duration can be longer than the lifetime of a given experiment, we still refer to this signal as *transient* since it originates from a transient astrophysical event. Furthermore, if a bosenova signal were to pass by the Earth, experiments running before and during the signal would be exposed to different ULDM field densities.

At the position of the detector, the burst can be characterized by a sum of plane waves of varying momenta k, as  $\phi_k(\vec{x}, t) \simeq \phi_{k,0} \cos{(E_{\phi}t + \vec{k} \cdot \vec{x})}$ . As a consequence, the emitted ULDM burst passing through the detector will deposit energy through the same interactions as cold DM. In particular, for nonderivative couplings that are linear in

 $\phi$ , as in Eq. (2), the sensitivity of a broadband DM experiment to a bosenova signal will follow characterization as in Ref. [60]. Taking the above effects into account, the sensitivity of a search for relativistic scalar fields,  $d_{i,*}$ , relative to a DM search sensitivity,  $d_i$ , at the same frequency by the ratio

$$\frac{d_{i,*}^{(1)}}{d_i^{(1)}} \sim \sqrt{\frac{\rho_{\rm DM}}{\rho_*}} \frac{t_{\rm int}^{1/4} \min(\tau_{\rm DM}^{1/4}, t_{\rm int}^{1/4})}{\min((\delta t)^{1/4}, t_{\rm int}^{1/4}) \min(\tau_*^{1/4}, t_{\rm int}^{1/4})}, \quad (31)$$

where  $t_{\rm int}$  is the integration time of the experiment. Note that the translation between frequency of the experiment and mass is slightly changed, since for virial DM the frequency of oscillation is  $\omega \approx m_{\phi}$ , whereas for the bosenova signal  $\omega \approx 2.6 m_{\phi}$ . We observe for example that for long burst duration  $(\delta t \gtrsim t_{\rm int})$  and long effective coherence time  $(\tau_* \to \tau_{\rm DM})$ , the sensitivity ratio is determined solely by the energy density in the burst  $\rho_*$  relative to the background DM density  $\rho_{\rm DM}$ . We will discuss the sensitivity  $d_{i,{\rm DM}}^{(1)}$  of current and future experimental searches in Sec. IV.

Finally, note that the analysis above only takes into account the leading relativistic peak in the ULDM emission spectrum, as in the analysis of Ref. [60]. This simplification allows one to capture qualitative behavior and the typical expected sensitivity reach. However, detailed analysis of the full emission spectrum from a given source, such as numerically computed in Ref. [58] for bosenova, can provide unique information about the underlying fundamental potential of ULDM beyond leading order that could be extracted in the event of a successful bosenova detection. We leave this for a dedicated study in the future.

## B. Bosenova rate

The event rate of bosenovae is sensitive to modeldependent cosmological and astrophysical assumptions, and hence is complicated with nontrivial estimates. To a first approximation, the rate depends on the intrinsic formation rate and distribution of boson stars at high redshift, the accretion [32,54,55,102] and merger [51-53] rate of boson stars, and details of the collapse and bosenova processes [57–59,103]. It should be noted that although we have focused on the well-studied example of boson star collapse, other ULDM systems are also expected to give rise to bosenovae, including superradiant clouds (discussed in Sec. II C 4) and gravitational atom configurations bound to astrophysical objects [91]. Importantly, as emphasized below, many experimental searches for ULDM will be automatically sensitive to the passage of a bosenova burst, without any change to their experiment and at most minor changes to their analysis pipeline. For this reason, we consider it reasonable to decouple the signal and rate estimates, focusing on the former here.

In the Appendix, we provide a very crude estimate of the rate under simplifying assumptions, which should be taken as illustrative only. While this issue is important and worthy of dedicated study in the future, it is far beyond the scope of this work, which focuses on the bosenova signal across a wide range of detector architectures. An additional discussion of the bosenova rate can be found in Ref. [60].

# IV. METHODS OF DETECTION

A variety of experimental setups and technology, especially those traditionally focusing on detecting scalar DM (see, e.g., [3]) and the variation of fundamental constants, constitute excellent laboratories for probing bursts of propagating relativistic ULDM particles. The sensitivity to couplings is further enhanced when the density of the scalar particles originating from a bosenova (or other) burst at the detector is larger than the ambient scalar particle DM density, in accordance with Eq. (31).

Various technologies for the detection of scalar DM have recently been reviewed in [3]. These include atomic, molecular, and nuclear clocks, as well as other spectroscopy experiments, optical cavities, atom interferometers, optical interferometers, torsion balances, mechanical resonators, and others. While here we are detecting the transient rather than continuous signal due to halo DM, the detection principles remain the same, and we only briefly review the sensitivities of relevant current and future detectors below.

## A. Atomic clocks

The coupling of the scalar DM to the SM leads to oscillations of fundamental constants [27], such as the fine-structure constant  $\alpha$ , proton-to-electron mass ratio  $\mu = m_p/m_e$ , and  $X_q = m_q/\Lambda_{\rm QCD}$  [104], where  $m_q$  is the average light quark mass, and  $\Lambda_{\text{QCD}}$  is the QCD scale. As atomic, molecular, and nuclear energy levels depends on values of fundamental constants, this effect leads to the variation of such energies, as well as the clock frequencies. Different types of clocks are sensitive to different fundamental constants. Moreover, clocks based on different transitions could have significantly different sensitivities; therefore, one observes a ratio of clock frequencies over time and extracts the signal via the discrete Fourier transform or power spectrum of the data [5–9,27]. The signal will persist for the duration of the burst. The bosenova burst would be detectable with various quantum clocks for a wide range of DM masses (being most sensitive for  $m \lesssim 10^{-13}$  eV) and interaction strengths.

## 1. Optical atomic clocks

The ratios of optical clock frequencies [105], i.e., based on transitions between different electronic levels (frequencies of  $0.4-1.1 \times 10^{15}$  Hz) are sensitive to photon [27] and hadronic sector [106] couplings. The frequency of the optical atomic clock can be expressed as [107]

$$\nu \sim cR_{\infty}AF(\alpha),$$
 (32)

where c is the speed of light, A is a numerical factor depending on an atom,  $F(\alpha)$  depends upon the particular transition, and  $R_{\infty}$  is the Rydberg constant. The sensitivity of optical atomic clocks to the variation of  $\alpha$  is parametrized by dimensionless sensitivity factors K that can be computed from first principles with high precision [108] and can be either positive or negative. Ultimate accuracy in the ability to detect the variation of the fundamental constant, and, therefore, ultralight scalar DM, depends on the difference in the sensitivity factors between two clocks and the achievable fractional accuracy of the ratio of frequencies  $\nu$ :

$$\frac{\partial}{\partial t} \ln \frac{\nu_2}{\nu_1} = (K_2 - K_1) \frac{1}{\alpha} \frac{\partial \alpha}{\partial t},\tag{33}$$

where indices 1 and 2 refer to clocks 1 and 2, respectively. The Yb<sup>+</sup> clock based on an electric octupole (E3)  $4f^{14}6s^2S_{1/2} \leftrightarrow 4f^{13}6s^2{}^2F_{7/2}$  transition has the largest (in magnitude) sensitivity factor K=-6 [108] among all presently operating clocks. The Yb<sup>+</sup> ions also support another clock transition based on the electric quadrupole (E2)  $4f^{14}6s^2S_{1/2} \leftrightarrow 4f^{14}5d^2D_{3/2}$  transition with K=1, and the  $^{171}$ Yb<sup>+</sup> E3/E2 clock-comparison pair presently provides the best limit for scalar DM for the lightest masses, with the experiment carried out by the PTB team [6].

Optical clocks based on highly charged ions (HCIs) [109] will have much larger sensitivities to the variation of  $\alpha$  than presently operating optical clocks. For example, a Cf<sup>15+</sup>/Cf<sup>17+</sup> pair has  $K_2 - K_1 > 100$  [110]. Development of HCI clocks is progressing rapidly, with a recent demonstration of an Ar<sup>13+</sup> clock with  $2 \times 10^{-17}$  uncertainty [111].

Recently, it was shown that coupling of ultralight scalar DM to quarks and gluons would lead to an oscillation of the nuclear charge radius detectable with optical atomic clocks [106,112], and their comparisons can be used to investigate DM-nuclear couplings, which were previously only accessible with other platforms.

The total electronic energy  $E_{\rm tot}$  of an atomic state contains the energies associated with the finite nucleus mass [mass shift] and the nonzero nuclear charge radius  $r_N$  [field shift (FS)], which dominated for heavy atoms and provides the better sensitivity. The field shift can be parametrized as

$$E_{\rm FS} \simeq K_{\rm FS} \langle r_N^2 \rangle$$
,

where  $K_{FS}$  is the field-shift constant leading to oscillation of the atomic energy due to the oscillation of the  $r_N$  caused by the coupling of nuclear sector to DM [106].

Therefore, measuring the ratio of two clock frequencies  $\nu_2$  and  $\nu_1$  of heavy atoms enables the detection of ultralight

DM that will cause the oscillation of  $r_N$ :

$$\frac{\Delta(\nu_2/\nu_1)}{(\nu_2/\nu_1)} = K_{2,1} \frac{\Delta\langle r_N^2 \rangle}{\langle r_N^2 \rangle}.$$
 (34)

We note that the sensitivity  $K_{2,1}$  of the clock pair to DM is different from the sensitivity to  $\alpha$  and is determined by the field shift constants of the clock transitions:

$$K_{2,1} \equiv \frac{K_{\rm FS}^{\nu_2} \langle r_N^2 \rangle}{\nu_2} - \frac{K_{\rm FS}^{\nu_1} \langle r_N^2 \rangle}{\nu_1}.$$

Corresponding limits on DM to coupling to gluons  $d_g$  and quarks  $d_{\hat{m}}$  are obtained as

$$\frac{\Delta(\nu_2/\nu_1)}{(\nu_2/\nu_1)} = K_{2,1}[(c_1+c_2)d_g + c_2d_{\hat{m}}]\sqrt{4\pi}\frac{\sqrt{2\rho_{\rm DM}}}{m_\phi M_{\rm pl}},$$

where  $c_1$  and  $c_2$  are of order unity (see Refs. [106,112]<sup>3</sup>). Interestingly, <sup>171</sup>Yb<sup>+</sup> E2/E3 clock pair has high sensitivity to this effect as well—upper states in these two clock transitions have significantly different electronic structure resulting in field shift constants that differ in sign. Yb is also quite heavy with Z = 70, and near-future experiments will allow improvement in a wide mass range [106].

## 2. Microwave clocks

Microwave clocks are based on transitions between hyperfine substates of the ground state of the atom (frequencies of a few GHz). The corresponding frequency of such with transitions can be expressed as [107]

$$\nu_{\rm hfs} \sim cR_{\infty}A_{\rm hfs} \times g_i \times \frac{m_{\rm e}}{m_{\rm p}} \times \alpha^2 F_{\rm hfs}(\alpha),$$
 (35)

where  $A_{\rm hfs}$  is a numerical quantity depending on a particular atom and  $F_{\rm hfs}(\alpha)$  is specific to each hyperfine transition. The dimensionless quantity  $g_i = \mu_i/(I\mu_{\rm N})$  is the nuclear g factor, where  $\mu_i$  is the nuclear magnetic moment, I is a nuclear spin, and  $\mu_{\rm N} = \frac{e\hbar}{2m_{\rm p}}$  is the nuclear magneton. The variation of g factors is commonly reduced to the variation of  $X_q = m_q/\Lambda_{\rm QCD}$  enabling sensitivity to DM-SM coupling to gluons  $d_q$  and quarks  $d_{\hat{m}}$ .

Comparing formulas given by Eqs. (32) and (35), we see that the ratio of microwave to optical clocks is sensitive to the various  $\alpha$ ,  $\mu$ , and  $X_q$  providing sensitivity to all linear couplings discussed in this work. The microwave Rb to Cs frequency clock ratio is sensitive to the variation of  $\alpha$  and  $X_q$  [107]:

<sup>&</sup>lt;sup>3</sup>The coefficients  $c_1$  and  $c_2$  were originally labeled as  $\alpha$  and  $\beta$  (respectively) in [106]. We have changed them here to avoid confusion with  $\alpha$ ,  $\alpha_s$ , and  $\beta(g_s)$ .

$$\frac{\nu_{\text{Cs}}}{\nu_{\text{Rh}}} = \frac{g_{\text{Cs}}}{g_{\text{Rh}}} \alpha^{0.49}; \tag{36}$$

see Refs. [104,113] for extraction of sensitivity to the nuclear sector from the g factors. Therefore, microwave clocks can probe all of the scalar DM couplings discussed here, but have reached their technical accuracy limit of  $10^{-16}$  [114], 2 orders of magnitude below the optical clocks. Rb/Cs clock-comparison limits are reported in [9].

# B. Molecular and nuclear clocks

Several new types of clocks are being developed (see reviews [3,113]), based on molecules and molecular ions [115,116], and the <sup>229</sup>Th nucleus [117].

Molecular clocks provide enhanced sensitivity to  $\mu$  variation and will allow a significantly improved sensitivity to electron couplings as well. For example, the linear triatomic molecule SrOH possesses a low-lying pair of near-degenerate vibrational states leading to a large sensitivity to changes in  $\mu$  and a high degree of control over systematic errors [118].

The design of a high precision optical clock requires the ability to construct a laser operating at the wavelength of the clock transition, which precludes using nuclear energy levels as their transition frequencies are generally outside of the laser-accessible range by many orders of magnitude. However, there is (so far) a single known exception, a nuclear transition that occurs between the long-lived (isomeric) first excited state of the <sup>229</sup>Th and the corresponding nuclear ground state, with a laser-accessible wavelength near 149 nm.

In 2023, the first observation of the radiative decay of the <sup>229</sup>Th nuclear clock isomer was reported [119], and the transition energy was measured to be 8.338(24) eV, corresponding to the photon vacuum wavelength of the isomer's decay of 148.71(42) nm. In 2024, laser excitation of Th-229 nuclear transition was demonstrated in Th-doped CaF<sub>2</sub> crystals using a tabletop tunable laser system [120]. The nuclear resonance for the Th<sup>4+</sup> ions in Th:CaF<sub>2</sub> is measured at the wavelength 148.3821(5) nm, with the fluorescence lifetime in the crystal being 630(15) s, corresponding to an isomer half-life of 1740(50) s for a nucleus isolated in vacuum.

The nuclear clock can be operated with a single Th<sup>3+</sup> trapped ion, much like a single ion atomic clock, except that it excites a nuclear rather than an atomic transition. Laser cooling of Th<sup>3+</sup> has already been demonstrated. An alternate solid-state scheme has also been suggested which cannot be implemented with atomic clocks (see the review [117] and references therein).

The nuclear clock is expected to have several orders of magnitude larger sensitivities to both the variation of  $\alpha$  and  $X_q$ , giving a unique opportunity to drastically enhance scalar ULDM searches, since the projected accuracy of

nuclear trapped ion clocks is  $10^{-19}$  [121]. Flambaum [122] suggested that the anomalously small transition energy of the  $^{229\text{m}}$ Th isomer is the result of a nearly perfect cancellation of a change in Coulomb energy,

$$\Delta E_C = E_C^{\rm m} - E_C \sim -1 \text{ MeV},$$

by opposite and nearly equal changes of the nuclear energy through the strong interaction; this is why both sensitivity to photon and nuclear couplings are similarly enhanced. This difference in the Coulomb energy and corresponding sensitivity to variation of  $\alpha$  can be estimated from the measured differences in the charge radii and quadrupole moments  $Q_0$  between the ground state and the isomer [123,124]:

$$\Delta E_C \approx -485 \text{ MeV} \left[ \frac{\langle r_{229\text{m}}^2 \rangle}{\langle r_{229}^2 \rangle} - 1 \right] + 11.6 \text{ MeV} [Q_0^{\text{m}}/Q_0 - 1]$$

$$= -0.29(43) \text{ MeV}, \tag{37}$$

which is limited by the accuracy in the  $Q_0^{\rm m}/Q_0$  value, but planned to be improved with a better ion trap [117]. The sensitivity value of  $K=-0.9(3)\times 10^4$  for  $\alpha$  sensitivity has been evaluated based on additional nuclear modeling that includes a relation between the change of the charge radius and that of the electric quadrupole moment [125]. Using this value, the sensitivity to the variation of  $\alpha$  and DM is determined the same way as for the atomic clock pair given by Eq. (32). A Th nuclear clock can be compared to any other atomic clock or a cavity. The sensitivity for the DM couplings of the hadronic sector is also  $\mathcal{O}(K)$ ; see [122]. The plans for the development of a nuclear clock have been discussed in detail in [117], and rapid progress is expected after a recent new measurement of the transition wavelength [119].

# C. Optical cavities

Variations of  $\alpha$  and particle masses also alter the geometric sizes of solid objects, scaling as  $L \propto a_{\rm B}$ , where  $a_{\rm B} = 1/(m_e \alpha)$  is the atomic Bohr radius [126,127] in the non-relativistic limit. When sound-wave propagation through the solid occurs sufficiently fast for a solid to fully respond to changes in the fundamental constants, the size of a solid body changes according to [3]:

$$\frac{\delta L}{L} \approx \frac{\delta a_{\rm B}}{a_{\rm B}} = -\frac{\delta \alpha}{\alpha} - \frac{\delta m_e}{m_e},\tag{38}$$

leading to the sensitivity to both photon and electron couplings.

Therefore, the cavity reference frequency  $\nu_{\text{cavity}} \propto 1/L$  can respond to changes in the fundamental constants, as [3,126,127]

$$\frac{\delta\nu_{\text{cavity}}}{\nu_{\text{cavity}}} = -\frac{\delta L}{L} \approx -\frac{\delta a_{\text{B}}}{a_{\text{B}}} = \frac{\delta \alpha}{\alpha} + \frac{\delta m_e}{m_e}$$
(39)

for the cavity whose length depends on the length of the solid spacer between the mirrors, enabling DM searches. One can compare the cavity reference frequency to the atomic frequency or to another cavity. We note that the atomic clock design includes an optical cavity, naturally supporting clock-cavity comparisons, as carried out in [11].

The size changes of the solid are enhanced if the oscillation frequency of the fundamental constants matches the frequency of a fundamental vibrational mode of the solid [3]. Various optical cavities can be used for ultralight scalar particle detection, with comparisons of atom-cavity [13] and cavity-cavity [12,16] comparisons setting limits on DM-SM couplings. Such experiments are naturally sensitive to DM mass ranges higher than that of clocks, complementing clock-clock comparisons as well as providing limits on additional couplings.

## D. Atom interferometers

In atom interferometry, laser pulses are used to coherently split, redirect, and recombine matter waves through stimulated absorption and emission of photons, driving transitions between the ground and a long-lived excited atomic state [128]. We note that a  ${}^{1}S_{0} - {}^{3}P_{0}$  narrow transition in Sr is used for both ultraprecise atomic clocks and atom interferometry schemes for future gravitational wave detection and DM searches [129].

Atom interferometers are sensitive to the oscillations of fundamental constants as well as DM-induced accelerations in dual-species interferometers, for example <sup>88</sup>Sr and <sup>87</sup>Sr. Such experiments compare the phase accumulated by delocalized atom clouds with DM affecting the atomic energies or exerting a force on the atom clouds, respectively.

Large-scale atom interferometers are required to enhance the sensitivity to DM. Large-scale 100-meter prototypes are currently being built [129]. Space-based atom interferometers (see AEDGE proposal [130]) will be highly sensitive to scalar and vector DM.

## E. Other detectors

Other spectroscopy DM limits include atomic Dy [18] and molecular iodine [16] experiments.

Ultralight DM may also exert time-varying forces on test bodies in optical inteferometers, but such forces are suppressed by the smallness of the electromagnetic and electron-mass contributions to the overall mass of a test body for scalar DM (see [3] for a brief review).

Torsion balances sense differential forces on macroscopic test masses. Although they were designed to test the EP [19], one can derive limits to scalar DM assuming that these particles create a differential force. The MICROSCOPE space mission tested the EP in orbit

using electrostatic accelerometers onboard a drag-free microsatellite [20]. We note that all limits derived from EP tests do not assume DM halo density, so these limits will not be affected by the enhanced density. This is because for linear couplings, the EP tests search for long-range Yukawa-type interactions, rather than the energy deposition from interactions with local DM fields. The EP tests are insensitive to the density of the DM nearby, and only test the long-range force between test masses. In the language of particle physics, the field potential arises at tree level, where a single virtual  $\phi$  is exchanged.

Various proposals recently reviewed in [3,131] use mechanical resonators spanning a range of frequencies from 1 Hz to 1 GHz, corresponding to a ULDM mass from  $10^{-14}$  eV to  $10^{-5}$  eV. These are naturally narrowband in DM mass.

# F. Networks of detectors on Earth and in space

One can use all of these experiments to set the limits on the bosenova bursts. The potential for significantly increased density of particles compared to halo DM leads to an increased chance of detection for all density-dependent experiments. One significant factor to consider is whether the experiment can reach its ultimate sensitivity during the burst, which we assume in all limits. Owing to vast differences in integration time to full sensitivity for different detection methods, we assume it can be achieved during the burst time in the present manuscript.

A network of detectors allows for better differentiation of burst signals from the local noise sources as well as improved precision [3]. Networks of detectors in space provide particularly interesting opportunities due to the large possible distances between network nodes. For example, the global positioning system (GPS) has been used to provide limits on transient DM effects [132]. A potentially tantalizing opportunity with the space network is the observation of the onset of the burst signal propagating through the network nodes and potential localization of the signal. Further work is needed for different detector types to explore these opportunities. Detecting the onset of relativistic bursts as opposed to nonrelativistic transients is a challenging prospect, but quantum technologies are improving rapidly, leading to significant improvements in both accuracy and stability. For example, the stability of optical lattice clocks has improved drastically in recent years, allowing us to reach  $10^{-18}$  uncertainties within a few minutes [133], with further orders of magnitude improvements possible.

Finally, note that a number of fundamental physics and DM studies with high-precision optical clocks in space have recently been proposed [134–136].

# V. RESULTS

We find that bursts of relativistic scalars offer a discovery reach orders of magnitude better than from background

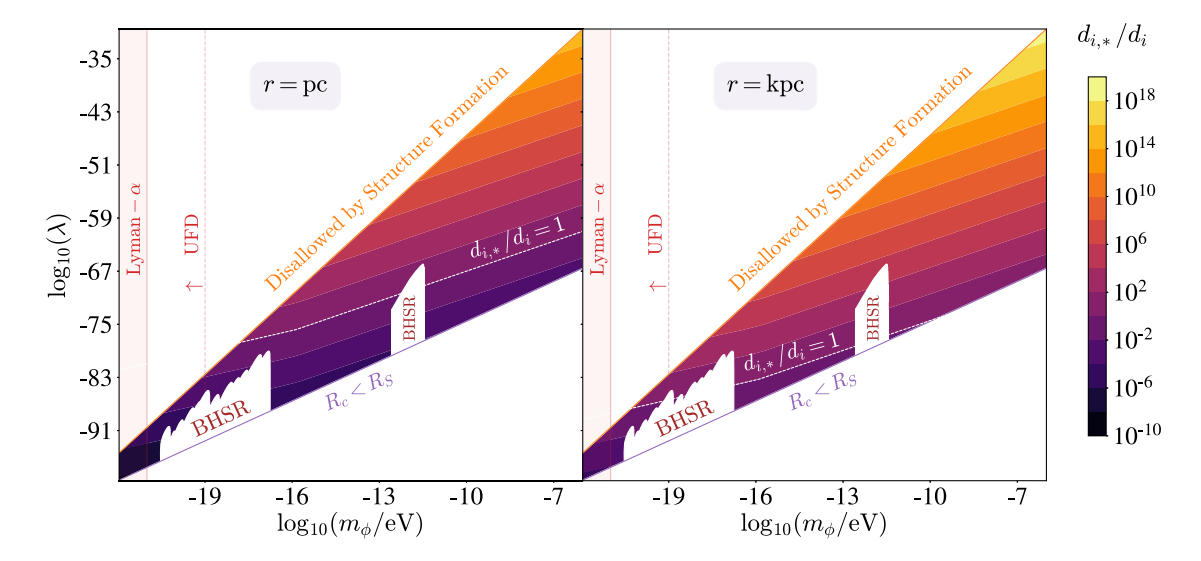


FIG. 5. The ratio of sensitivity to a given coupling for a burst search  $d_{i,*}$  relative to a DM search  $d_i$ , for the allowed parameter space in  $m_{\phi}$  vs  $\lambda$ ; the white dotted line corresponds to equal sensitivity to bursts and DM. We illustrate two choices of distance to the bosenova: r = pc (left) and r = kpc (right). See Sec. II C and Fig. 1 for discussion of constraints.

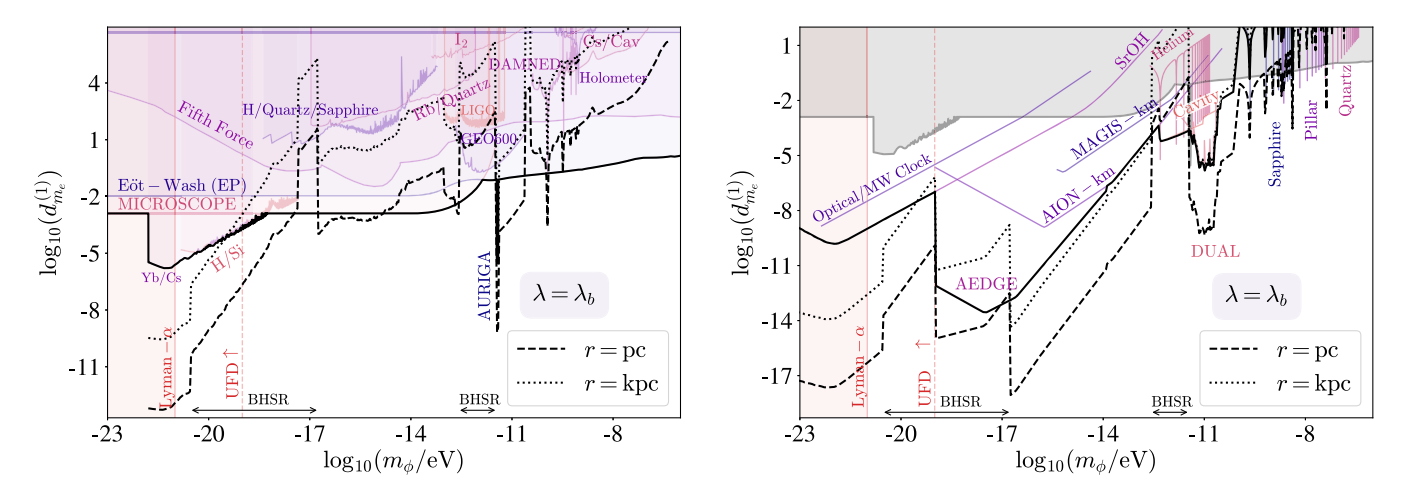


FIG. 6. Bounds on  $d_{m_e}^{(1)}$  as a function of  $m_\phi$  from current experiments (left) and projections for future experiments (right). In both plots, the solid black lines trace the best bound for each mass. The dashed and dotted black lines represent the potential reach for detecting bosenovae at distances of r=pc and kpc, respectively. We choose  $\lambda=\lambda_b$  in Eq. (40), as explained in the text. Current experiments consist of various detector types. *Clocks:* frequency comparison between <sup>171</sup>Yb optical lattice clock and <sup>133</sup>Cs fountain microwave clock (Yb/Cs) [8]. *Optical cavities:* H-maser comparison with a Si cavity (H/Si) [11], comparison between Cs clock and a cavity (Cs/Cav) [12], and comparison of a H-maser and sapphire oscillator with a quartz oscillator (H/Quartz/Sapphire) [13]. *Optical interferometers:* unequal delay interferometer experiment (DAMNED) [14], colocated Michelson interferometers (Holometer) [15], Spectroscopy: molecular iodine spectroscopy (I2) [16], comparison between <sup>87</sup>Rb hyperfine transition and quartz mechanical oscillator (Rb/Quartz) [17]. Equivalence principle tests: searches for EP violation (Eöt-Wash [19] and MICROSCOPE [20]). *Mechanical oscillators:* resonant mass detector (AURIGA) [21]. Fifth force tests: fifth force searches looking for deviations from the gravitational inverse square law [23]. Gravitational wave detectors: (GEO 600 [24], LIGO O3 [25]). Future experiments include optical/microwave clock comparison (Optical/MW) [27], SrOH molecular spectroscopy [118], atom interferometery (terrestrial MAGIS [129], and space-based AEDGE and AION [130]), resonant-mass detectors [DUAL [137]) and other mechanical resonators (sapphire, pillar, quartz and superfluid helium [138]]. UFDs [87] and Lyman- $\alpha$  [85,86] also constrain ULDM. Finally, the regions of the parameter space corresponding to the BHSR bounds [88,89] are displayed at the bottom of the plots by the arrows (note the discontinuity in  $\lambda_b$  in this range).

DM over a range of bosenova distances r, scalar masses  $m_{\phi}$ , and self-interaction couplings  $\lambda$ . In Fig. 5, we show contours of the potential reach of the coupling ratio,  $d_{i,*}^{(1)}/d_i^{(1)}$  with  $i=e,m_e,g$ , over the  $m_{\phi}-\lambda$  plane. We

calculate the coupling ratio using Eq. (31), with burst density given by Eq. (28) and the burst timescales in Eqs. (29) and (30). Since the distance to the bosenova is a free parameter (for our purposes), we take two benchmarks

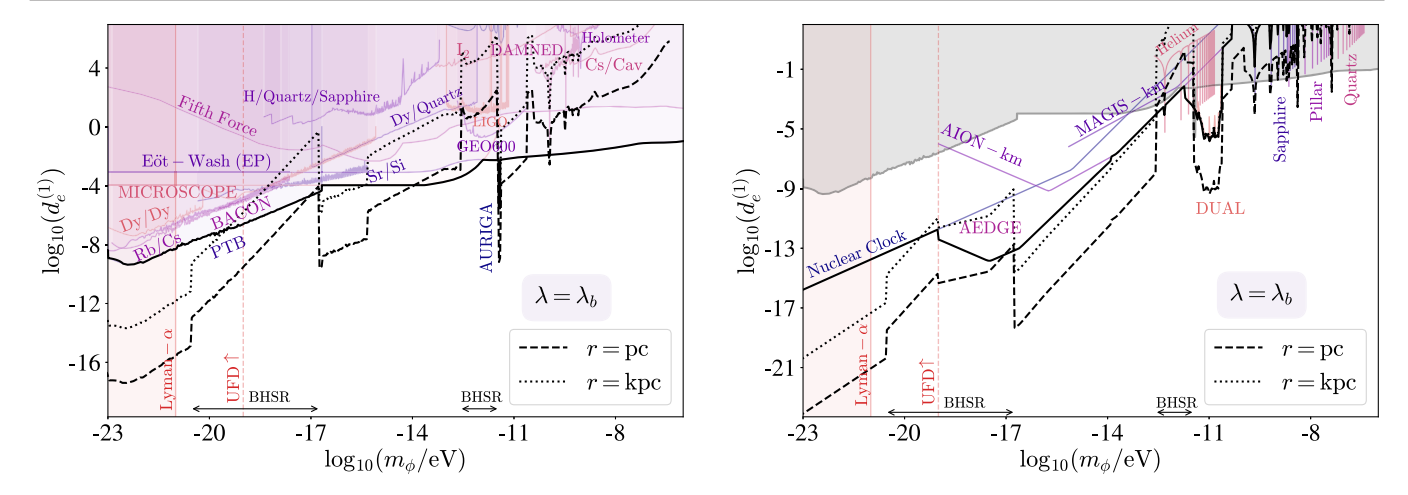


FIG. 7. Bounds on  $d_e$  as a function of  $m_{\phi}$  from current experiments (left) and projections for proposed experiments (right). In both plots, the solid black lines trace the best bound for each mass. The dashed and dotted black lines represent the potential reach for detecting bosenovae at distances of r = pc and kpc, respectively. We choose  $\lambda = \lambda_b$  in Eq. (40), as explained in the text. Current experiments include the following. Clocks: frequency ratios of <sup>27</sup>Al<sup>+</sup>, <sup>171</sup>Yb, and <sup>87</sup>Sr optical clocks (BACON) [5], frequency ratios of single-ion <sup>171</sup>Yb<sup>+</sup> clock and <sup>87</sup>Sr optical lattice clock (PTB) [6], ratio of frequencies of atomic clocks based on <sup>171</sup>Yb<sup>+</sup> and <sup>87</sup>Sr (Yb+/Sr) [7], and dual <sup>133</sup>Cs/<sup>87</sup>Rb atomic fountain clock frequency ratio (Rb/Cs) [9]. Optical cavities: frequency comparisons between strontium optical clock and silicon cavity (Sr/Si) [11], atomic spectroscopy in cesium vapor with Fabry-Perot cavity locked to laser (Cs/Cav) [12] and frequency comparision of hydrogen maser and sapphire oscillator with quartz oscillator (H/Quartz/Sapphire) [13]. Optical interferometers: three-arm Mach-Zender interferometer (DAMNED) [14] and colocated Michelson interferometers (Holometer) [15]. Spectroscopy: spectroscopic experiments of molecular iodine (I<sub>2</sub>) [16], frequency comparison of <sup>164</sup>Dy with quartz oscillator (Dy/ Quartz) [17], precision spectroscopy measurements involving two isotopes of dysprosium (Dy/Dy) [18]. Equivalence principle tests: tests of equivalence principle violation by (Eöt-Wash) [19] and (MICROSCOPE) [20]. Mechanical resonators: resonant mass detector (AURIGA) [21]. Gravitational wave detectors (GEO 600) [24] and (LIGO O3) [25]. Future experiments include thorium nuclear clock projections [3], space-based atom interferometers (AEDGE and AION) [130], terrestrial atom interferometers (MAGIS) [129], resonant-mass detectors DUAL [137], and mechanical resonators (sapphire, pillar, quartz and superfluid helium) [138]. UFDs [87] and Lyman- $\alpha$  [85,86] also constrain ULDM. Finally, the regions of the parameter space corresponding to the BHSR bounds [88,89] are displayed at the bottom of the plots by the arrows (note the discontinuity in  $\lambda_b$  in this range).

of r=1 pc (left) and r=1 kpc (right) to capture a range of possible Galactic sources. This coupling ratio is independent of the specifics of the experiment in question, and therefore provides a blueprint for the most interesting parameter space for current and future experiments. As in Fig. 1, the relevant parameter space is limited by Lyman- $\alpha$  [85,86] and UFDs [87] and structure formation considerations (see Sec. II C 2), as well as at small  $\lambda$  by the limitations of the nonrelativistic analysis [see Eq. (23)].

The dotted white line in Fig. 5 represents where  $d_{i,*}^{(1)}/d_i^{(1)}=1$ , i.e., the coupling that can be probed by detecting a bosenova at a distance r is the same as that of background DM. Modulo the timing factors of Eq. (31), this in essence says that the density of scalars from the burst is the same as the background DM. Regions below this contour represent  $d_{i,*}^{(1)}/d_i^{(1)}<1$ , which means that the coupling that can be probed in those regions of the parameter space are smaller than those that can be probed by signals from background DM. In other words, below this line the bosenovae are most advantageous.

Figure 5 can be used to translate an experiment's sensitivity to background DM into a sensitivity to a bosenova by multiplying the experimental coupling reach by the coupling ratio  $d_{i,*}/d_i$ . The recipe to translate a DM limit to a burst limit in a given experiment is as follows: for a given mass range  $m_{\phi}$  that the experiment is sensitive to, choose a value of  $\lambda$  that is allowed in that mass range. Then the coupling reach can be determined by multiplying the DM limit on  $d_i^{(1)}$  by the value of the  $d_{i,*}^{(1)}/d_i^{(1)}$  over that  $\lambda$  slice. For instance, if an experiment was sensitive to DM masses of  $10^{-19}$ – $10^{-16}$  eV, a viable benchmark for  $\lambda$ could be, e.g.,  $10^{-85}$ . For a bosenova with these parameters, the coupling ratio  $d_{i,*}^{(1)}/d_i^{(1)}$  is  $\mathcal{O}(10^{-3})$  for a distance of r = 1 pc. This means that, in the presence of a bosenova, the sensitivity for the burst signal covers 3 additional orders of magnitude compared to the background DM limit.

Figures 6–8 show the reach of the  $d_{m_e}^{(1)}$ ,  $d_e^{(1)}$ , and  $d_g^{(1)}$ , respectively, as a function of  $m_{\phi}$ . We display the reach for both current experiments (left) and proposed future experiments (right). For this parameter space, there are two

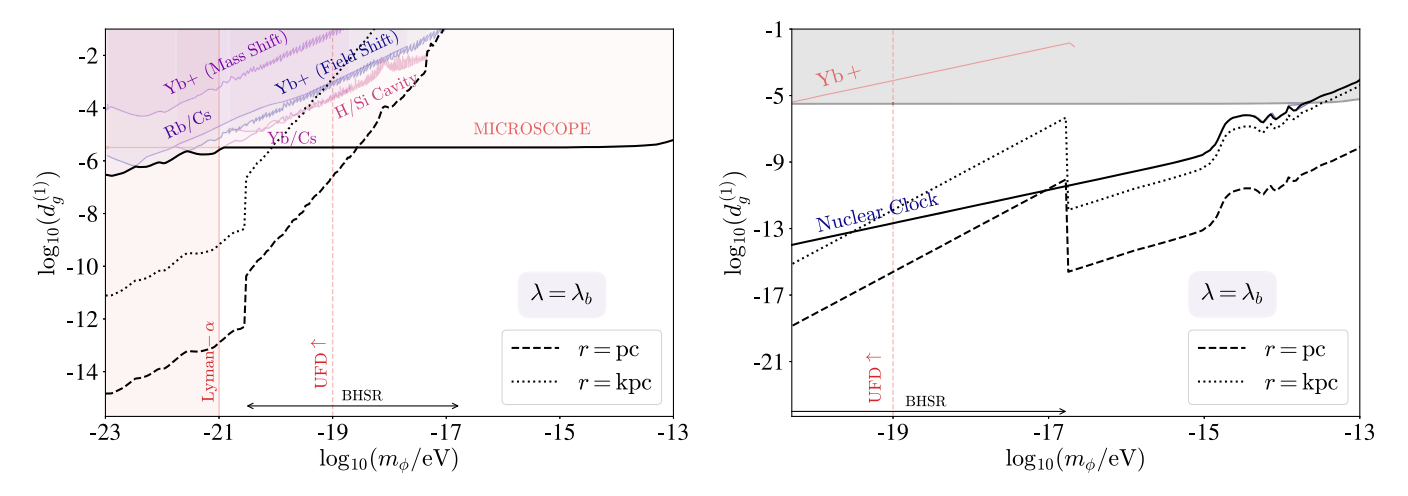


FIG. 8. Bounds on  $d_g$  as a function of  $m_\phi$  from current experiments (left) and projections for proposed experiments (right). In both plots, the solid black lines traces the best bound for each mass. The dashed and dotted black lines represent the potential reach for detecting bosenovae at distances of r= pc and kpc, respectively. We choose  $\lambda=\lambda_b$  in Eq. (40), as explained in the text. Experiments that are sensitive to  $d_g^{(1)}$  include the following. *Clocks*: <sup>171</sup>Yb lattice clock—<sup>133</sup>Cs microwave clock comparison (Yb/Cs) [8] and frequency comparison in dual rubidium-caesium cold atom clock (Rb/Cs) [9]. *Optical cavities*: H-maser comparison with a Si cavity (H/Si) [11]. *Equivalence principle tests*: MICROSCOPE [20], while future experiment projections are for the <sup>229</sup>Th nuclear clock [3] and <sup>171</sup>Yb<sup>+</sup> ion clock [106]. UFDs [87] and Lyman- $\alpha$  [85,86] also constrain ULDM. Finally, the regions of the parameter space corresponding to the BHSR bounds [88,89] are displayed at the bottom of the plots by the arrows (note the discontinuity in  $\lambda_b$  in this range).

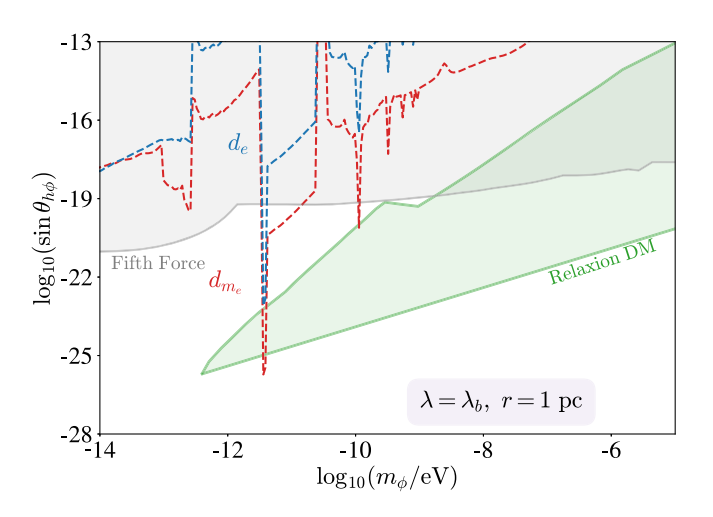
additional parameters: the self coupling  $\lambda$  and bosenova distance r. As before, each figure shows two benchmark distances of r = 1 pc and r = 1 kpc.

Since  $\rho_* \propto 1/\lambda$  [see Eq. (28)], smaller values of  $\lambda$  will increase detection prospects. Taking into account all of the constraints on  $\lambda$  laid out in Sec. II C, we choose values of  $\lambda$  at each mass which will maximize the size of the signal. The benchmark  $\lambda_b$  is chosen therefore to trace right above the lower bounds on  $\lambda$ , as shown by the black dashed line in

Fig. 1. This benchmark choice is defined piecewise by

$$\lambda_{\rm b} = \begin{cases} 3 \times 10^{-73} \left(\frac{m_{\phi}}{10^{-13} \, {\rm eV}}\right)^{6} & 10^{-13} \lesssim \frac{m_{\phi}}{\rm eV} \lesssim 10^{-12} \\ 10^{-90} \left(\frac{m_{\phi}}{5 \times 10^{-21} \, {\rm eV}}\right)^{4} & 10^{-21} \lesssim \frac{m_{\phi}}{\rm eV} \lesssim 10^{-17} \,. \end{cases}$$
(40)  
$$10\lambda_{\rm BH} \qquad \text{elsewhere}$$

For the regions in Fig. 1 not dominated by black hole superradiance bounds, we take  $\lambda = 10\lambda_{BH}$  to safely ignore



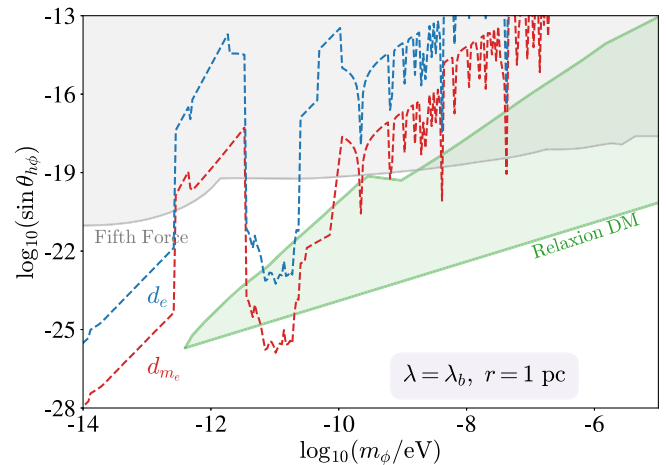


FIG. 9. The reach for the bosenova search compared to the relaxion DM parameter space (green shaded region [71]), for current experiments (left) and future experiments (right). The strongest current constraints, derived from EP and fifth force experiments, are represented by the light gray region. The potential reach for bosenova searches for  $d_{m_e}$  and  $d_e$  are shown by the red and blue dashed lines and derived using Eq. (18) from the experiments listed in Figs. 6 and 7 (respectively). The bosenovae were taken to be at a benchmark distance of r = pc.

relativistic effects that would arise and modify the dynamics of the bosenovae. We emphasize that this benchmark is chosen by hand based on existing constraints, and the precise form was not derived from any theoretical considerations.

Finally, we illustrate a dedicated relaxion parameter space in Fig. 9. We display the parameter space in terms of the Higgs-relaxion mixing parameter,  $\sin\theta_{h\phi}$ , which is related to the dilatonic couplings via Eq. (18). With upcoming experiments probing  $d_e$  and  $d_{m_e}$ , there will be significant potential to probe well-motivated relaxion DM parameter space.

Finally, we note that although the parameter space  $m_{\phi} \lesssim 10^{-19} \; \mathrm{eV}$  is already constrained by astrophysics and cosmology (especially UFDs and Lyman- $\alpha$ ), laboratory searches are still useful and complementary in this range. Laboratory and astrophysical probes are based on very different assumptions and therefore provide useful confirmation of one another. Furthermore, in models where the ULDM scalar field is a subleading fraction  $f \lesssim 0.1$  of the total DM density, astrophysical constraints can disappear completely, whereas laboratory searches typically reduce sensitivity by only  $\sqrt{f}$ . In fact, in the present context, the total ULDM density only affects the rate of bosenovae, but not the size of a given bosenova signal if it does occur.

## VI. CONCLUSIONS AND OUTLOOK

ULDM can form compact objects that eventually collapse and explode, resulting in transient burst emissions of relativistic scalar fields. This can lead to distinct observational signatures compared to Galactic DM. We have demonstrated that current experiments searching for DM couplings to photons, electrons, and gluons may already be sensitive to such bosenova signals. Upcoming experiments and technology, including nuclear clocks as well as spacebased interferometers, will be able to sensitively probe orders of magnitude in the ULDM coupling-mass parameter space.

The search for transient bursts of relativistic scalars is a new field of study, which gives rise to unique strategies for detecting DM. Not only can the ULDM density be enhanced during the transit of a burst, but a detection of a bosenova signal can also provide important insight into the fundamental self-interaction potential of  $\phi$ , which is otherwise very difficult to probe. This is because the emission spectrum of the bosenova depends on this potential. The analysis put forth in our work is general, and the methodology can be readily applied to other astrophysical sources of relativistic scalar fields. Scalar particle emission can generally originate from hot and dense environments. Our work also opens up new

avenues for multimessenger astronomy associated with new physics as well. For instance, if the bosenova collapse exhibits a quadrupole moment in its mass distribution, then it is possible for there to be a detectable gravitational wave signal. Additionally, the dilatonic coupling to photons could lead to radio emission from boson stars, a phenomenon which has been studied in the context of axion stars [103]. We leave the exploration of these ideas for future work.

Since the properties of the bosenova are linked to  $m_{\phi}$  and  $\lambda$ , other transient sources could have a distinct dependence on these parameters, and therefore lead to different detection prospects. In particular, in the event of a bosenova detection, the pattern of peaks in the emission spectrum may encode important information about the underlying UV physics, which is inaccessible in an ordinary DM search. A dedicated study of the emission spectrum of bosenovae in theories with different scalar field potentials is therefore highly motivated.

# ACKNOWLEDGMENTS

We thank Abhishek Banerjee, Masha Baryakhtar, and John Ellis for useful discussions. This work was supported in part by the NSF QLCI Award No. OMA-2016244, NSF Grants No. PHY-2012068 and No. PHY-2309254, and the European Research Council (ERC) under the European Union's Horizon 2020 research and innovation program (Grant No. 856415). J. A. thanks the International Center for Quantum-field Measurement Systems for Studies of the Universe and Particles (QUP) for the hospitality and exciting research environment. The work of J. E. and V. T. was supported by the World Premier International Research Center Initiative (WPI), MEXT, Japan, and by the KAKENHI Grants No. 21H05451 No. 21K20366 (J. E.), and No. 23K13109 (V. T.). This research was supported in part by the INT's U.S. Department of Energy Grant No. DE-FG02-00ER41132.

# APPENDIX: APPROXIMATION OF BOSENOVA RATE

As emphasized in the main text, the rate of boson star collapse leading to bosenova is an important but complex issue, which depends on numerous model-dependent assumptions. We postpone a dedicated study of this rate to future work. As a first, very crude approximation, we illustrate how such a calculation might be done below, though the reader should not interpret the result as a concrete estimate.

For the purpose of illustration, we employ the ansatz of a fixed boson star mass  $M=M_c$  and assume a homogeneous distribution around the Galaxy, taking the fraction of DM in boson stars to be  $f_{\rm DM} \leq 1$ . In this case, the average distance  $\bar{r}$  between boson stars is

<sup>&</sup>lt;sup>4</sup>For example, such as that found in astrophysical settings of neutron star mergers [139,140].

$$\bar{r} \sim \left(\frac{3M_c}{4\pi f_{\rm DM}\rho_{\rm DM}}\right)^{1/3} \approx \frac{30~{\rm pc}}{f_{\rm DM}^{1/3}} \left(\frac{10^{-80}}{\lambda}\right)^{1/6}.$$
 (A1)

This estimate would imply a total number of boson stars

$$N_{\rm bs} \sim 4 \times 10^7 f_{\rm DM} \left(\frac{\lambda}{10^{-80}}\right)^{1/2} \left(\frac{r}{10 \text{ kpc}}\right)^3$$
 (A2)

in a galaxy of size ~10 kpc (e.g., the Milky Way).

As mentioned above, the average rate of bosenova signals is complicated with significant uncertainties (see [60,141] for some discussion). Let us consider an approximate simplified example. Suppose one boson star collapse occurs on average every  $T \sim \text{Gyr}$  within a given galaxy. Note that this choice is not the output of any calculation, but is only used here for illustration. Then using the estimate in Eq. (A2), the rate of bosenovae within a distance r of Earth would be of order

$$\Gamma \sim \frac{N_{\rm bs}}{T} \sim 0.04 \text{ year}^{-1} \left(\frac{\lambda}{10^{-80}}\right)^{1/2} \left(\frac{r}{10 \text{ kpc}}\right)^3.$$
 (A3)

Therefore, this highly simplistic example implies a rate of one bosenova every 25 years in the Milky Way.

For comparison, the supernova rate in the Milky Way is estimated at roughly 1 per 50 years [142]. Calculations of expected event rates for bosenovae from merging axion stars and axion miniclusters have been found to be as large as ~3 bosenovae per day in the Milky Way [143]. While there is significant uncertainty, this further highlights that bosenovae can carry significant implications and warrant further study for which we lay the groundwork.

It is also worth noting in this context that other ULDM systems can give rise to bosenovae. Superradiant clouds of ULDM around black holes, discussed in Sec. II C 4, have been predicted to be destabilized by self-interactions, leading to collapse and bosenova explosion [95], although more recent work suggests the possibility of a steady-state configuration at late times [88,98]. Additionally, ULDM can be captured around astrophysical objects, including stars, with density that grows exponentially [91]; in addition to terrestrial signals from a solar halo [144,145], the collapse of these gravitational atoms is expected to also end with a bosenova. A complete picture of the bosenova rate in the Galaxy should self-consistently take all of these possibilities into account. We postpone further discussion and improved estimates of the bosenova rates in each of these systems for future work.

<sup>[1]</sup> G. Bertone, D. Hooper, and J. Silk, Particle dark matter: Evidence, candidates and constraints, Phys. Rep. **405**, 279 (2005).

<sup>[2]</sup> D. F. J. Kimball and K. van Bibber, *The Search for Ultralight Bosonic Dark Matter* (Springer, Cham, 2023).

<sup>[3]</sup> D. Antypas *et al.*, New horizons: Scalar and vector ultralight dark matter, arXiv:2203.14915.

<sup>[4]</sup> C. B. Adams et al., Axion dark matter, arXiv:2203.14923.

<sup>[5]</sup> BACON Collaboration, Frequency ratio measurements at 18-digit accuracy using an optical clock network, Nature (London) 591, 564 (2021).

<sup>[6]</sup> M. Filzinger, S. Dörscher, R. Lange, J. Klose, M. Steinel, E. Benkler, E. Peik, C. Lisdat, and N. Huntemann, Improved limits on the coupling of ultralight bosonic dark matter to photons from optical atomic clock comparisons, Phys. Rev. Lett. 130, 253001 (2023).

<sup>[7]</sup> N. Sherrill *et al.*, Analysis of atomic-clock data to constrain variations of fundamental constants, New J. Phys. **25**, 093012 (2023).

<sup>[8]</sup> T. Kobayashi, A. Takamizawa, D. Akamatsu, A. Kawasaki, A. Nishiyama, K. Hosaka *et al.*, Search for ultralight dark matter from long-term frequency comparisons of optical and microwave atomic clocks, Phys. Rev. Lett. 129, 241301 (2022).

<sup>[9]</sup> A. Hees, J. Guéna, M. Abgrall, S. Bize, and P. Wolf, Searching for an oscillating massive scalar field as a dark

matter candidate using atomic hyperfine frequency comparisons, Phys. Rev. Lett. **117**, 061301 (2016).

<sup>[10]</sup> S. Aharony, N. Akerman, R. Ozeri, G. Perez, I. Savoray, and R. Shaniv, Constraining rapidly oscillating scalar dark matter using dynamic decoupling, Phys. Rev. D 103, 075017 (2021).

<sup>[11]</sup> C. J. Kennedy, E. Oelker, J. M. Robinson, T. Bothwell, D. Kedar, W. R. Milner, G. Edward Marti, A. Derevianko, and J. Ye, Precision metrology meets cosmology: Improved constraints on ultralight dark matter from atom-cavity frequency comparisons, Phys. Rev. Lett. 125, 201302 (2020).

<sup>[12]</sup> O. Tretiak, X. Zhang, N. L. Figueroa, D. Antypas, A. Brogna, A. Banerjee, G. Perez, and D. Budker, Improved bounds on ultralight scalar dark matter in the radio-frequency range, Phys. Rev. Lett. 129, 031301 (2022).

<sup>[13]</sup> W. M. Campbell, B. T. McAllister, M. Goryachev, E. N. Ivanov, and M. E. Tobar, Searching for scalar dark matter via coupling to fundamental constants with photonic, atomic and mechanical oscillators, Phys. Rev. Lett. **126**, 071301 (2021).

<sup>[14]</sup> E. Savalle, A. Hees, F. Frank, E. Cantin, P.-E. Pottie, B. M. Roberts, L. Cros, B. T. McAllister, and P. Wolf, Searching for dark matter with an optical cavity and an unequal-delay interferometer, Phys. Rev. Lett. 126, 051301 (2021).

- [15] L. Aiello, J. W. Richardson, S. M. Vermeulen, H. Grote, C. Hogan, O. Kwon, and C. Stoughton, Constraints on scalar field dark matter from colocated Michelson interferometers, Phys. Rev. Lett. 128, 121101 (2022).
- [16] R. Oswald *et al.*, Search for dark-matter-induced oscillations of fundamental constants using molecular spectroscopy, Phys. Rev. Lett. **129**, 031302 (2022).
- [17] X. Zhang, A. Banerjee, M. Leyser, G. Perez, S. Schiller, D. Budker, and D. Antypas, Search for ultralight dark matter with spectroscopy of radio-frequency atomic transitions, Phys. Rev. Lett. 130, 251002 (2023).
- [18] K. Van Tilburg, N. Leefer, L. Bougas, and D. Budker, Search for ultralight scalar dark matter with atomic spectroscopy, Phys. Rev. Lett. **115**, 011802 (2015).
- [19] A. Hees, O. Minazzoli, E. Savalle, Y. V. Stadnik, and P. Wolf, Violation of the equivalence principle from light scalar dark matter, Phys. Rev. D 98, 064051 (2018).
- [20] J. Bergé, P. Brax, G. Métris, M. Pernot-Borràs, P. Touboul, and J.-P. Uzan, MICROSCOPE Mission: First constraints on the violation of the weak equivalence principle by a light scalar dilaton, Phys. Rev. Lett. 120, 141101 (2018).
- [21] A. Branca *et al.*, Search for an ultralight scalar dark matter candidate with the AURIGA detector, Phys. Rev. Lett. **118**, 021302 (2017).
- [22] E. Fischbach and C. Talmadge, Ten years of the fifth force, in 31st Rencontres de Moriond: Dark Matter and Cosmology, Quantum Measurements and Experimental Gravitation (1996), pp. 443–451, arXiv:hep-ph/9606249.
- [23] J. Murata and S. Tanaka, A review of short-range gravity experiments in the LHC era, Classical Quantum Gravity **32**, 033001 (2015).
- [24] S. M. Vermeulen *et al.*, Direct limits for scalar field dark matter from a gravitational-wave detector, Nature (London) **600**, 424 (2021).
- [25] K. Fukusumi, S. Morisaki, and T. Suyama, Upper limit on scalar field dark matter from LIGO-Virgo third observation run, Phys. Rev. D 108, 095054 (2023).
- [26] E. G. Adelberger, B. R. Heckel, and A. E. Nelson, Tests of the gravitational inverse square law, Annu. Rev. Nucl. Part. Sci. 53, 77 (2003).
- [27] A. Arvanitaki, J. Huang, and K. Van Tilburg, Searching for dilaton dark matter with atomic clocks, Phys. Rev. D 91, 015015 (2015).
- [28] D. J. Kaup and Klein-Gordon Geon, Klein-Gordon geon, Phys. Rev. **172**, 1331 (1968).
- [29] R. Ruffini and S. Bonazzola, Systems of self-gravitating particles in general relativity and the concept of an equation of state, Phys. Rev. **187**, 1767 (1969).
- [30] M. Colpi, S. Shapiro, and I. Wasserman, Boson stars: Gravitational equilibria of self-interacting scalar fields, Phys. Rev. Lett. **57**, 2485 (1986).
- [31] D. Levkov, A. Panin, and I. Tkachev, Gravitational Bose-Einstein condensation in the kinetic regime, Phys. Rev. Lett. **121**, 151301 (2018).
- [32] J. Chen, X. Du, E. W. Lentz, D. J. E. Marsh, and J. C. Niemeyer, New insights into the formation and growth of boson stars in dark matter halos, Phys. Rev. D 104, 083022 (2021).

- [33] K. Kirkpatrick, A. E. Mirasola, and C. Prescod-Weinstein, Relaxation times for Bose-Einstein condensation in axion miniclusters, Phys. Rev. D 102, 103012 (2020).
- [34] J. Chen, X. Du, E. W. Lentz, and D. J. E. Marsh, Relaxation times for Bose-Einstein condensation by self-interaction and gravity, Phys. Rev. D **106**, 023009 (2022).
- [35] K. Kirkpatrick, A. E. Mirasola, and C. Prescod-Weinstein, Analysis of Bose-Einstein condensation times for selfinteracting scalar dark matter, Phys. Rev. D 106, 043512 (2022).
- [36] E. Seidel and W.-M. Suen, Dynamical evolution of boson stars. 1. Perturbing the ground state, Phys. Rev. D 42, 384 (1990).
- [37] P.-H. Chavanis, Mass-radius relation of Newtonian self-gravitating Bose-Einstein condensates with short-range interactions: I. Analytical results, Phys. Rev. D 84, 043531 (2011).
- [38] P. Chavanis and L. Delfini, Mass-radius relation of Newtonian self-gravitating Bose-Einstein condensates with short-range interactions: II. Numerical results, Phys. Rev. D 84, 043532 (2011).
- [39] J. Eby, P. Suranyi, C. Vaz, and L. Wijewardhana, Axion stars in the infrared limit, J. High Energy Phys. 03 (2015) 080.
- [40] M. P. Hertzberg, Quantum radiation of oscillons, Phys. Rev. D 82, 045022 (2010).
- [41] J. Eby, P. Suranyi, and L. C. R. Wijewardhana, The lifetime of axion stars, Mod. Phys. Lett. A 31, 1650090 (2016).
- [42] K. Mukaida, M. Takimoto, and M. Yamada, On longevity of I-ball/oscillon, J. High Energy Phys. 03 (2017) 122.
- [43] E. Braaten, A. Mohapatra, and H. Zhang, Emission of photons and relativistic axions from axion stars, Phys. Rev. D 96, 031901 (2017).
- [44] J. Eby, M. Ma, P. Suranyi, and L. Wijewardhana, Decay of ultralight axion condensates, J. High Energy Phys. 01 (2018) 066.
- [45] H.-Y. Zhang, M. A. Amin, E. J. Copeland, P. M. Saffin, and K. D. Lozanov, Classical decay rates of oscillons, J. Cosmol. Astropart. Phys. 07 (2020) 055.
- [46] M. P. Hertzberg, F. Rompineve, and J. Yang, Decay of boson stars with application to glueballs and other real scalars, Phys. Rev. D 103, 023536 (2021).
- [47] J. Eby, L. Street, P. Suranyi, and L. C. R. Wijewardhana, Global view of axion stars with nearly Planck-scale decay constants, Phys. Rev. D **103**, 063043 (2021).
- [48] B. C. Mundim, A numerical study of boson star binaries, Ph.D. thesis, British Columbia University, 2010.
- [49] E. Cotner, Collisional interactions between self-interacting nonrelativistic boson stars: Effective potential analysis and numerical simulations, Phys. Rev. D **94**, 063503 (2016).
- [50] B. Schwabe, J. C. Niemeyer, and J. F. Engels, Simulations of solitonic core mergers in ultralight axion dark matter cosmologies, Phys. Rev. D 94, 043513 (2016).
- [51] J. Eby, M. Leembruggen, J. Leeney, P. Suranyi, and L. C. R. Wijewardhana, Collisions of dark matter axion stars with astrophysical sources, J. High Energy Phys. 04 (2017) 099.
- [52] M. P. Hertzberg, Y. Li, and E. D. Schiappacasse, Merger of dark matter axion clumps and resonant photon emission, J. Cosmol. Astropart. Phys. 07 (2020) 067.

- [53] X. Du, D. J. E. Marsh, M. Escudero, A. Benson, D. Blas, C. K. Pooni, and M. Fairbairn, Soliton merger rates and enhanced axion dark matter decay, Phys. Rev. D 109, 043019 (2024).
- [54] J. H.-H. Chan, S. Sibiryakov, and W. Xue, Condensation and evaporation of boson stars, J. High Energy Phys. 01 (2024) 071.
- [55] A. S. Dmitriev, D. G. Levkov, A. G. Panin, and I. I. Tkachev, Self-similar growth of Bose stars, Phys. Rev. Lett. 132, 091001 (2024).
- [56] T. Helfer, D. J. E. Marsh, K. Clough, M. Fairbairn, E. A. Lim, and R. Becerril, Black hole formation from axion stars, J. Cosmol. Astropart. Phys. 03 (2017) 055.
- [57] J. Eby, M. Leembruggen, P. Suranyi, and L. C. R. Wijewardhana, Collapse of axion stars, J. High Energy Phys. 12 (2016) 066.
- [58] D. G. Levkov, A. G. Panin, and I. I. Tkachev, Relativistic axions from collapsing Bose stars, Phys. Rev. Lett. 118, 011301 (2017).
- [59] J. Eby, M. Leembruggen, P. Suranyi, and L. C. R. Wijewardhana, QCD axion star collapse with the chiral potential, J. High Energy Phys. 06 (2017) 014.
- [60] J. Eby, S. Shirai, Y. V. Stadnik, and V. Takhistov, Probing relativistic axions from transient astrophysical sources, Phys. Lett. B 825, 136858 (2022).
- [61] P. Sikivie, N. Sullivan, and D. B. Tanner, Proposal for axion dark matter detection using an LC circuit, Phys. Rev. Lett. 112, 131301 (2014).
- [62] Y. Kahn, B. R. Safdi, and J. Thaler, Broadband and resonant approaches to axion dark matter detection, Phys. Rev. Lett. 117, 141801 (2016).
- [63] J. L. Ouellet *et al.*, First results from ABRACADABRA-10 cm: A search for Sub-μeV axion dark matter, Phys. Rev. Lett. **122**, 121802 (2019).
- [64] C. P. Salemi et al., Search for low-mass axion dark matter with ABRACADABRA-10 cm, Phys. Rev. Lett. 127, 081801 (2021).
- [65] A. V. Gramolin, D. Aybas, D. Johnson, J. Adam, and A. O. Sushkov, Search for axion-like dark matter with ferromagnets, Nat. Phys. 17, 79 (2021).
- [66] M. Silva-Feaver *et al.*, Design overview of DM radio pathfinder experiment, IEEE Trans. Appl. Supercond. **27**, 1400204 (2017).
- [67] DMRadio Collaboration, Status of DMRadio-50L and DMRadio-m<sup>3</sup>, SciPost Phys. Proc. **12**, 036 (2023).
- [68] DMRadio Collaboration, Electromagnetic modeling and science reach of DMRadio-m³, arXiv:2302.14084.
- [69] P. W. Graham, D. E. Kaplan, and S. Rajendran, Cosmological relaxation of the electroweak scale, Phys. Rev. Lett. 115, 221801 (2015).
- [70] A. Banerjee, H. Kim, and G. Perez, Coherent relaxion dark matter, Phys. Rev. D 100, 115026 (2019).
- [71] A. Chatrchyan and G. Servant, Relaxion dark matter from stochastic misalignment, J. Cosmol. Astropart. Phys. 06 (2023) 036.
- [72] A. Banerjee, G. Perez, M. Safronova, I. Savoray, and A. Shalit, The phenomenology of quadratically coupled ultra light dark matter, J. High Energy Phys. 10 (2023) 042.

- [73] T. Bouley, P. Sorensen, and T.-T. Yu, Constraints on ultralight scalar dark matter with quadratic couplings, J. High Energy Phys. 03 (2023) 104.
- [74] J. Fan, Ultralight repulsive dark matter and BEC, Phys. Dark Universe **14**, 84 (2016).
- [75] G. Grilli di Cortona, E. Hardy, J. Pardo Vega, and G. Villadoro, The QCD axion, precisely, J. High Energy Phys. 01 (2016) 034.
- [76] W. H. Press, B. S. Ryden, and D. N. Spergel, Single mechanism for generating large scale structure and providing dark missing matter, Phys. Rev. Lett. 64, 1084 (1990).
- [77] S.-J. Sin, Late time cosmological phase transition and galactic halo as Bose liquid, Phys. Rev. D 50, 3650 (1994).
- [78] W. Hu, R. Barkana, and A. Gruzinov, Cold and fuzzy dark matter, Phys. Rev. Lett. 85, 1158 (2000).
- [79] P. J. E. Peebles, Fluid dark matter, Astrophys. J. 534, L127 (2000).
- [80] L. Amendola and R. Barbieri, Dark matter from an ultralight pseudo-Goldsone-boson, Phys. Lett. B 642, 192 (2006).
- [81] L. Hui, J. P. Ostriker, S. Tremaine, and E. Witten, Ultralight scalars as cosmological dark matter, Phys. Rev. D 95, 043541 (2017).
- [82] E. G. M. Ferreira, Ultra-light dark matter, Astron. Astrophys. Rev. 29, 7 (2021).
- [83] M. Markevitch, A. H. Gonzalez, D. Clowe, A. Vikhlinin, L. David, W. Forman, C. Jones, S. Murray, and W. Tucker, Direct constraints on the dark matter self-interaction crosssection from the merging galaxy cluster 1E0657-56, Astrophys. J. 606, 819 (2004).
- [84] J. A. R. Cembranos, A. L. Maroto, S. J. Núñez Jareño, and H. Villarrubia-Rojo, Constraints on anharmonic corrections of fuzzy dark matter, J. High Energy Phys. 08 (2018) 073.
- [85] V. Iršič, M. Viel, M. G. Haehnelt, J. S. Bolton, and G. D. Becker, First constraints on fuzzy dark matter from Lyman- $\alpha$  forest data and hydrodynamical simulations, Phys. Rev. Lett. **119**, 031302 (2017).
- [86] K. K. Rogers and H. V. Peiris, Strong bound on canonical ultralight axion dark matter from the Lyman-Alpha forest, Phys. Rev. Lett. 126, 071302 (2021).
- [87] N. Dalal and A. Kravtsov, Excluding fuzzy dark matter with sizes and stellar kinematics of ultrafaint dwarf galaxies, Phys. Rev. D 106, 063517 (2022).
- [88] M. Baryakhtar, M. Galanis, R. Lasenby, and O. Simon, Black hole superradiance of self-interacting scalar fields, Phys. Rev. D 103, 095019 (2021).
- [89] C. Ünal, F. Pacucci, and A. Loeb, Properties of ultralight bosons from heavy quasar spins via superradiance, J. Cosmol. Astropart. Phys. 05 (2021) 007.
- [90] D. Dutta Chowdhury, F. C. van den Bosch, P. van Dokkum, V. H. Robles, H.-Y. Schive, and T. Chiueh, On the dynamical heating of dwarf galaxies in a fuzzy dark matter halo, Astrophys. J. 949, 68 (2023).
- [91] D. Budker, J. Eby, M. Gorghetto, M. Jiang, and G. Perez, A generic formation mechanism of ultralight dark matter solar halos, J. Cosmol. Astropart. Phys. 12 (2023) 021.

- [92] S. Chakrabarti, B. Dave, K. Dutta, and G. Goswami, Constraints on the mass and self-coupling of ultra-light scalar field dark matter using observational limits on galactic central mass, J. Cosmol. Astropart. Phys. 09 (2022) 074.
- [93] E. Y. Davies and P. Mocz, Fuzzy dark matter soliton cores around supermassive black holes, Mon. Not. R. Astron. Soc. 492, 5721 (2020).
- [94] N. Craig, Naturalness: A Snowmass White Paper, Eur. Phys. J. C 83, 825 (2023).
- [95] A. Arvanitaki and S. Dubovsky, Exploring the string axiverse with precision black hole physics, Phys. Rev. D 83, 044026 (2011).
- [96] A. Arvanitaki, M. Baryakhtar, and X. Huang, Discovering the QCD axion with black holes and gravitational waves, Phys. Rev. D 91, 084011 (2015).
- [97] A. Arvanitaki, M. Baryakhtar, S. Dimopoulos, S. Dubovsky, and R. Lasenby, Black hole mergers and the QCD axion at Advanced LIGO, Phys. Rev. D 95, 043001 (2017).
- [98] N. P. Branco, R. Z. Ferreira, and J. a. G. Rosa, Superradiant axion clouds around asteroid-mass primordial black holes, J. Cosmol. Astropart. Phys. 04 (2023) 003.
- [99] T. Flacke, C. Frugiuele, E. Fuchs, R. S. Gupta, and G. Perez, Phenomenology of relaxion-Higgs mixing, J. High Energy Phys. 06 (2017) 050.
- [100] A. H. Guth, M. P. Hertzberg, and C. Prescod-Weinstein, Do dark matter axions form a condensate with long-range correlation?, Phys. Rev. D 92, 103513 (2015).
- [101] J. Eby, M. Leembruggen, L. Street, P. Suranyi, and L. C. R. Wijewardhana, Approximation methods in the study of boson stars, Phys. Rev. D 98, 123013 (2018).
- [102] B. Eggemeier and J. C. Niemeyer, Formation and mass growth of axion stars in axion miniclusters, Phys. Rev. D 100, 063528 (2019).
- [103] D. G. Levkov, A. G. Panin, and I. I. Tkachev, Radioemission of axion stars, Phys. Rev. D 102, 023501 (2020).
- [104] V. V. Flambaum and A. F. Tedesco, Dependence of nuclear magnetic moments on quark masses and limits on temporal variation of fundamental constants from atomic clock experiments, Phys. Rev. C 73, 055501 (2006).
- [105] A. D. Ludlow, M. M. Boyd, J. Ye, E. Peik, and P. O. Schmidt, Optical atomic clocks, Rev. Mod. Phys. 87, 637 (2015).
- [106] A. Banerjee, D. Budker, M. Filzinger, N. Huntemann, G. Paz, G. Perez *et al.*, Oscillating nuclear charge radii as sensors for ultralight dark matter, arXiv:2301.10784.
- [107] M. Safronova, D. Budker, D. DeMille, D. F. J. Kimball, A. Derevianko, and C. W. Clark, Search for new physics with atoms and molecules, Rev. Mod. Phys. 90, 025008 (2018).
- [108] V. V. Flambaum and V. A. Dzuba, Search for variation of the fundamental constants in atomic, molecular, and nuclear spectra, Can. J. Phys. 87, 25 (2009).
- [109] M. G. Kozlov, M. S. Safronova, J. R. Crespo López-Urrutia, and P. O. Schmidt, Highly charged ions: Optical clocks and applications in fundamental physics, Rev. Mod. Phys. 90, 045005 (2018).
- [110] S. G. Porsev, U. I. Safronova, M. S. Safronova, P. O. Schmidt, A. I. Bondarev, M. G. Kozlov, I. I. Tupitsyn,

- and C. Cheung, Optical clocks based on the  $Cf^{15+}$  and  $Cf^{17+}$  ions, Phys. Rev. A **102**, 012802 (2020).
- [111] S. A. King, L. J. Spieß, P. Micke, A. Wilzewski, T. Leopold, E. Benkler *et al.*, An optical atomic clock based on a highly charged ion, Nature (London) **611**, 43 (2022).
- [112] V. V. Flambaum and A. J. Mansour, Variation of the quadrupole hyperfine structure and nuclear radius due to an interaction with scalar and axion dark matter, Phys. Rev. Lett. **131**, 113004 (2023).
- [113] M. S. Safronova, The search for variation of fundamental constants with clocks, Ann. Phys. (Berlin) 531, 1800364 (2019).
- [114] S. Weyers, V. Gerginov, M. Kazda, J. Rahm, B. Lipphardt, G. Dobrev, and K. Gibble, Advances in the accuracy, stability, and reliability of the PTB primary fountain clocks, Metrologia 55, 789 (2018).
- [115] D. Hanneke, B. Kuzhan, and A. Lunstad, Optical clocks based on molecular vibrations as probes of variation of the proton-to-electron mass ratio, Quantum Sci. Technol. 6, 014005 (2021).
- [116] S. S. Kondov, C.-H. Lee, K. H. Leung, C. Liedl, I. Majewska, R. Moszynski, and T. Zelevinsky, Molecular lattice clock with long vibrational coherence, Nat. Phys. 15, 1118 (2019).
- [117] E. Peik, T. Schumm, M. S. Safronova, A. Pálffy, J. Weitenberg, and P. G. Thirolf, Nuclear clocks for testing fundamental physics, Quantum Sci. Technol. 6, 034002 (2021).
- [118] I. Kozyryev, Z. Lasner, and J. M. Doyle, Enhanced sensitivity to ultralight bosonic dark matter in the spectra of the linear radical SrOH, Phys. Rev. A **103**, 043313 (2021).
- [119] S. Kraemer, J. Moens, M. Athanasakis-Kaklamanakis, S. Bara, K. Beeks, P. Chhetri *et al.*, Observation of the radiative decay of the <sup>229</sup>Th nuclear clock isomer, Nature (London) **617**, 706 (2023).
- [120] J. Tiedau, M. V. Okhapkin, K. Zhang, J. Thielking, G. Zitzer, E. Peik *et al.*, Laser excitation of the Th-229 nucleus, Phys. Rev. Lett. **132**, 182501 (2024).
- [121] C. J. Campbell, A. G. Radnaev, A. Kuzmich, V. A. Dzuba, V. V. Flambaum, and A. Derevianko, Single-ion nuclear clock for metrology at the 19th decimal place, Phys. Rev. Lett. 108, 120802 (2012).
- [122] V. V. Flambaum, Enhanced effect of temporal variation of the fine structure constant and the strong interaction in <sup>229</sup>Th, Phys. Rev. Lett. **97**, 092502 (2006).
- [123] J. C. Berengut, V. A. Dzuba, V. V. Flambaum, and S. G. Porsev, Proposed experimental method to determine  $\alpha$  sensitivity of splitting between ground and 7.6 eV isomeric states in <sup>229</sup>Th, Phys. Rev. Lett. **102**, 210801 (2009).
- [124] J. Thielking, M. V. Okhapkin, P. Glowacki, D. M. Meier, L. von der Wense, B. Seiferle, C. E. Düllmann, P. G. Thirolf, and E. Peik, Laser spectroscopic characterization of the nuclear-clock isomer <sup>229m</sup>Th, Nature (London) 556, 321 (2018).
- [125] P. Fadeev, J. C. Berengut, and V. V. Flambaum, Sensitivity of <sup>229</sup>Th nuclear clock transition to variation of the fine-structure constant, Phys. Rev. A **102**, 052833 (2020).
- [126] Y. V. Stadnik and V. V. Flambaum, Searching for dark matter and variation of fundamental constants with laser

- and maser interferometry, Phys. Rev. Lett. **114**, 161301 (2015).
- [127] Y. V. Stadnik and V. V. Flambaum, Enhanced effects of variation of the fundamental constants in laser interferometers and application to dark-matter detection, Phys. Rev. A 93, 063630 (2016).
- [128] O. Buchmueller, D. Carney, T. Cecil, J. Ellis, R. F. G. Ruiz, A. A. Geraci *et al.*, Snowmass 2021: Quantum sensors for HEP science—interferometers, mechanics, traps, and clocks, arXiv:2203.07250.
- [129] M. Abe, P. Adamson, M. Borcean, D. Bortoletto, K. Bridges, S. P. Carman *et al.*, Matter-wave atomic gradiometer interferometric sensor (MAGIS-100), Quantum Sci. Technol. **6**, 044003 (2021).
- [130] L. Badurina, O. Buchmueller, J. Ellis, M. Lewicki, C. McCabe, and V. Vaskonen, Prospective sensitivities of atom interferometers to gravitational waves and ultralight dark matter, Phil. Trans. R. Soc. A 380, 20210060 (2021).
- [131] D. Carney, G. Krnjaic, D. C. Moore, C. A. Regal, G. Afek, S. Bhave *et al.*, Mechanical quantum sensing in the search for dark matter, Quantum Sci. Technol. 6, 024002 (2021).
- [132] B. M. Roberts, G. Blewitt, C. Dailey, M. Murphy, M. Pospelov, A. Rollings, J. Sherman, W. Williams, and A. Derevianko, Search for domain wall dark matter with atomic clocks on board global positioning system satellites, Nat. Commun. 8, 1195 (2017).
- [133] T. Bothwell, C. J. Kennedy, A. Aeppli, D. Kedar, J. M. Robinson, E. Oelker, A. Staron, and J. Ye, Resolving the gravitational redshift across a millimetre-scale atomic sample, Nature (London) **602**, 420 (2022).
- [134] Y.-D. Tsai, J. Eby, and M. S. Safronova, Direct detection of ultralight dark matter bound to the Sun with space quantum sensors, Nat. Astron. 7, 113 (2023).
- [135] A. Derevianko, K. Gibble, L. Hollberg, N. R. Newbury, C. Oates, M. S. Safronova, L. C. Sinclair, and N. Yu,

- Fundamental physics with a state-of-the-art optical clock in space, Quantum Sci. Technol. 7, 044002 (2022).
- [136] V. Schkolnik, D. Budker, O. Fartmann, V. Flambaum, L. Hollberg, T. Kalaydzhyan *et al.*, Optical atomic clock aboard an Earth-orbiting space station (OACESS): Enhancing searches for physics beyond the standard model in space, Quantum Sci. Technol. 8, 014003 (2023).
- [137] A. Arvanitaki, S. Dimopoulos, and K. Van Tilburg, Sound of dark matter: Searching for light scalars with resonant-mass detectors, Phys. Rev. Lett. 116, 031102 (2016).
- [138] J. Manley, D. Wilson, R. Stump, D. Grin, and S. Singh, Searching for scalar dark matter with compact mechanical resonators, Phys. Rev. Lett. 124, 151301 (2020).
- [139] S. P. Harris, J.-F. Fortin, K. Sinha, and M. G. Alford, Axions in neutron star mergers, J. Cosmol. Astropart. Phys. 07 (2020) 023.
- [140] D. F. G. Fiorillo and F. Iocco, Axions from neutron star mergers, Phys. Rev. D 105, 123007 (2022).
- [141] M. Escudero, C. K. Pooni, M. Fairbairn, D. Blas, X. Du, and D. J. E. Marsh, Axion star explosions: A new source for axion indirect detection, Phys. Rev. D 109, 043018 (2024).
- [142] K. Rozwadowska, F. Vissani, and E. Cappellaro, On the rate of core collapse supernovae in the Milky Way, New Astron. 83, 101498 (2021).
- [143] D. Maseizik and G. Sigl, Distributions and collision rates of ALP stars in the Milky Way, arXiv:2404.07908.
- [144] A. Banerjee, D. Budker, J. Eby, H. Kim, and G. Perez, Relaxion stars and their detection via atomic physics, Commun. Phys. **3**, 1 (2020).
- [145] A. Banerjee, D. Budker, J. Eby, V. V. Flambaum, H. Kim, O. Matsedonskyi, and Gilad Perez, Searching for Earth/solar axion halos, J. High Energy Phys. 09 (2020) 004.